# MORE DIAGNOSIS OF SOLAR FLARE PROBABILITY FROM CHROMOSPHERE IMAGE SEQUENCES

**Donald C. Norquist and K. S. Balasubramaniam**

**28 September 2012**

**Interim Report**

**AIR FORCE RESEARCH LABORATORY**
**Space Vehicles Directorate**
**3550 Aberdeen Ave SE**
**AIR FORCE MATERIEL COMMAND**
**Kirtland AFB, MA 87117-5776**

# DTIC COPY
# NOTICE AND SIGNATURE PAGE

AFRL-RV-PS-TR-2012-0194 HAS BEEN REVIEWED AND IS APPROVED FOR PUBLICATION IN ACCORDANCE WITH ASSIGNED DISTRIBUTION STATEMENT.


//signed//                                      //signed//

_____     _____
Donald C. Norquist                              Edward J. Masterson, Colonel, USAF
Project Manager, AFRL/RVBXS                      Chief, AFRL/RVB

# REPORT DOCUMENTATION PAGE

*Form Approved*
*OMB No. 0704-0188*

| 1. REPORT DATE *(DD-MM-YYYY)* 28-09-2012 | 2. REPORT TYPE Interim Report | 3. DATES COVERED *(From - To)* 1 Oct 2011 to 07 Sep 2012 |
|---|---|---|

**4. TITLE AND SUBTITLE**
More Diagnosis of Solar Flare Probability from Chromosphere Image Sequences

**5a. CONTRACT NUMBER**

**5b. GRANT NUMBER**

**5c. PROGRAM ELEMENT NUMBER**
62601F

**6. AUTHOR(S)**
Donald C. Norquist and K. S. Balasubramaniam

**5d. PROJECT NUMBER**
1010

**5e. TASK NUMBER**
PPM00004579

**5f. WORK UNIT NUMBER**
EF004380

**7. PERFORMING ORGANIZATION NAME(S) AND ADDRESS(ES)**
Air Force Research Laboratory
Space Vehicles Directorate
3550 Aberdeen Avenue SE
Kirtland AFB, NM 87117-5776

**8. PERFORMING ORGANIZATION REPORT NUMBER**
AFRL-RV-PS-TR-2012-0194

**9. SPONSORING / MONITORING AGENCY NAME(S) AND ADDRESS(ES)**

**10. SPONSOR/MONITOR'S ACRONYM(S)**
AFRL/RVBXS

**11. SPONSOR/MONITOR'S REPORT NUMBER(S)**

**12. DISTRIBUTION / AVAILABILITY STATEMENT**

Approved for public release; distribution is unlimited. (377ABW-2012-1263 dtd 21 Sep 12)

**13. SUPPLEMENTARY NOTES**

**14. ABSTRACT**
This report describes a continuation of the work reported in AFRL-RV-PS-TP-2012-0005. First, we nearly doubled the original set of 46 ISOON Hα image sequences to 90. Second, the flare probability diagnosis algorithm was modified from the last version in the previous report to use the 1-minute image time change of the leading eigenvectors as predictors, and flaring level indicators prescribed from the whole sequence eigenvector patterns and the x-ray flux rise as predictors. Third, a new approach was investigated that attempted a single flare probability diagnosis for the whole image sequence. Frequency of occurrence of 1-minute eigenvector changes for an entire sequence over a designated number of size bins served as the predictor vector elements for each sequence, and the sequence-prescribed flaring level indicator was the predictand. Fourth, the latter method was limited to using occurrence frequency over just the pre-flare image times. The three new methods and the legacy algorithm were evaluated using three development sets of 60 sequences to train the candidate algorithm, and the applying resulting discriminant vectors to the three application sets of 30 independent sequences. The first two methods, which diagnosed flare category probability at individual image times, performed the best. Lastly, we investigated augmentation of Hα eigenvectors with ISOON Doppler velocity eigenvectors to see if flare category discrimination could be improved.

**15. SUBJECT TERMS**
Solar flares, optical images, x-ray flux, flare probability, principle component analysis, multivariate discriminant analysis

| 16. SECURITY CLASSIFICATION OF: | | | 17. LIMITATION OF ABSTRACT | 18. NUMBER OF PAGES | 19a. NAME OF RESPONSIBLE PERSON Donald C. Norquist |
|---|---|---|---|---|---|
| a. REPORT UNCLASSIFIED | b. ABSTRACT UNCLASSIFIED | c. THIS PAGE UNCLASSIFIED | Unlimited | 54 | 19b. TELEPHONE NUMBER *(include area code)* |

**Standard Form 298 (Rev. 8-98)**
**Prescribed by ANSI Std. 239.18**

This page is intentionally left blank.

# Table of Contents

# List of Figures

# List of Tables

# Acknowledgements

# 1. INTRODUCTION

This study was a continuation of the applied research project reported by Norquist and Balasubramaniam [1]. We continued our investigation of the utility of optical observations of the solar chromosphere in the diagnosis of flare probability. Because we felt we were not ready to project the flare probability estimate ahead in time, we stayed with our focus on inferring flaring likelihood at the observation time. As in the previous study, we used observed hydrogen-alpha (Hα) intensity from the U. S. Air Force Improved Solar Observing Optical Network (ISOON) telescope at Sacramento Peak, NM (Neidig et al. [2]). Sequences of Hα images at one-minute intervals and one arc second grid spacing for selected sub-regions of solar active regions over 5-10 hour periods comprised the data set. We performed principal component analysis (PCA) on the sequences to derive the eigenvectors and associated eigenvalues. Sub-region average Hα intensity and whole disk 1-8 Å x-ray flux from the NOAA Geostationary Operational Environmental Satellite (GOES) determined a flaring degree category at each image time. A subset of leading eigenvector elements at each time served as the predictors and flaring category constituted the predictand in employing multivariate discriminant analysis (MVDA). We invoked MVDA on selected image sequences making up a "development set." We then applied resulting discriminant vectors to the eigenvector elements of "application set" sequences to determine flaring category probability at observation times. Comparison of diagnosed probability with specified flaring category over all application times determined the diagnosis skill.

We began the new period of study by adding ISOON image sequences so that more would be available to the flare diagnosis development and application algorithms. By acquiring an additional 44 image sequences for specific date-active region sub-regions, we expanded our available pool of images sequences to 90. In the previous study, we found that the image sequences could be partitioned by flaring level indicator (FLI) according to the temporal pattern of the leading eigenvectors and the corresponding x-ray flux rise associated with any flare present in the sequence. Norquist and Balasubramaniam [1] predetermined the FLI for each ISOON sequence based on a subjective assessment of its Hα eigenvector patterns and the associated x-ray flux peak value. We continued that approach to determine the FLI for the new sequences added in the present study period. Briefly, the four FLI values were described as follows: FLI = 0 for no flare above x-ray background and smoothly varying (sinusoidal) eigenvectors; FLI = 1 for weak flares (peak flux in the x-ray decade of the background value) with spiked otherwise smoothly varying (sinusoidal) eigenvectors; FLI = 2 for moderate x-ray flares (one decade greater than background) and smoothly curved (non-sinusoidal) eigenvectors before and after the flare spike; FLI = 3 for strong x-ray flares (two or more decades above background) with non-curving eigenvectors before and smoothly curving after sharp spikes. In FLI = 1-3, the eigenvector spike occurs at the same time as the sharp rise in the x-ray flux. There must be a simultaneous eigenvector spike and a clear x-ray flux rise in order for a non-zero FLI category to be assigned to an image sequence. For reference, see Figure 7 of Norquist and Balasubramaniam [1] for examples of each FLI category. In Table 1 we list the 90 image sequences distributed into three image sequence sets (ISS) that have an approximately equal number of each of the FLI categories. In Table 1, Date is given in YYYYMMDD format, AR # is NOAA active region number (if assigned to the active region at time of observation), and FLI is prescribed flaring level indicator. Combinations of these three ISS served as development and application sets in the present study.

1

**Table 1. ISOON Hα Image Sequence Sets (ISS) Used In This Study**

| ISS 1 | | | ISS 2 | | | ISS 3 | | |
|---|---|---|---|---|---|---|---|---|
| Date | AR # | FLI | Date | AR # | FLI | Date | AR # | FLI |
| 20021213 | 10213 | 1 | 20021213 | 10215 | 1 | 20021213 | 10220 | 1 |
| 20021213 | 10223 | 1 | 20030102 | 10234 | 0 | 20030102 | 10239 | 0 |
| 20021213 | 10224 | 0 | 20030117 | 10254 | 0 | 20030117 | 10255 | 0 |
| 20021219 | 10229 | 3 | 20030117 | 10257 | 0 | 20030117 | 10259 | 0 |
| 20030117 | 10250 | 0 | 20030117 | 10258 | 1 | 20030203 | 10274 | 0 |
| 20030117 | 10256 | 0 | 20030203 | 10272 | 0 | 20030206 | ----- | 1 |
| 20030117 | 10260 | 0 | 20030318 | 10318 | 0 | 20030318 | 10319 | 0 |
| 20030203 | 10276 | 0 | 20030331 | 10321 | 0 | 20030331 | 10324 | 0 |
| 20030318 | 10323 | 0 | 20030331 | 10326 | 1 | 20030401 | 10318 | 1 |
| 20030331 | 10323 | 1 | 20030401 | 10321 | 0 | 20030401 | 10325 | 0 |
| 20030331 | 10325 | 0 | 20030401 | 10323 | 1 | 20030509 | ----- | 1 |
| 20030401 | 10319 | 1 | 20030513 | 10358 | 0 | 20030516 | 10357 | 0 |
| 20030401 | 10326 | 0 | 20030522 | 10362 | 1 | 20030528 | 10365 | 1 |
| 20030516 | 10356 | 1 | 20030605 | 10373 | 0 | 20030605 | 10375 | 0 |
| 20030528 | 10368 | 1 | 20030606 | ----- | 0 | 20030606 | 10377 | 1 |
| 20030604 | 10373 | 0 | 20030606 | 10375 | 1 | 20030610 | 10375 | 0 |
| 20030606 | 10373 | 0 | 20030610 | 10380 | 0 | 20030611 | 10375 | 2 |
| 20030609 | 10375 | 1 | 20030611 | 10375 | 2 | 20030611 | 10377 | 0 |
| 20030610 | 10377 | 0 | 20030612 | 10375 | 1 | 20030612 | 10380 | 0 |
| 20030611 | 10380 | 2 | 20030612 | 10377 | 0 | 20030613 | 10380 | 1 |
| 20030611 | 10381 | 0 | 20030613 | 10377 | 0 | 20030616 | 10380 | 0 |
| 20030612 | 10381 | 0 | 20030620 | 10385 | 0 | 20030620 | 10387 | 0 |
| 20030616 | 10385 | 0 | 20030623 | 10386 | 0 | 20030623 | 10387 | 0 |
| 20030620 | 10386 | 1 | 20030623 | 10397 | 0 | 20030624 | 10386 | 0 |
| 20030620 | 10388 | 0 | 20030624 | 10387 | 1 | 20031031 | 10488 | 1 |
| 20030623 | 10388 | 0 | 20030625 | 10391 | 0 | 20031104 | 10486 | 3 |
| 20030624 | 10390 | 0 | 20031029 | 10486 | 3 | 20040105 | ----- | 1 |
| 20031104 | 10486 | 1 | 20031104 | 10486 | 1 | 20040316 | ----- | 0 |
| 20041007 | ----- | 0 | 20041109 | 10696 | 2 | 20050506 | 10758 | 2 |
| 20050513 | 10759 | 3 | 20050909 | 10808 | 3 | 20061206 | 10930 | 3 |

In the balance of this report, we describe several methods involving four-category MVDA that used predictor vectors and prescribed predictands derived from Hα intensity and x-ray flux data at individual image times of the image sequences in Table 1.  In Section 2, we briefly review the best performing version of the flare probability diagnosis development and application algorithms from the previous study. In Section 3, we describe modifications to that algorithm pair made to attempt to improve discrimination among the flaring categories. In Section 4 we relate the results of the evaluation of the two image time flare probability diagnosis methods. In Section 5 we describe a technique to diagnose flaring for each image sequence as a whole, and present the results of its assessment. In Section 6 we discuss the modification of the whole-

sequence method and present its results. In Section 7 we relate our preliminary consideration of using Doppler velocity data from ISOON as a possible supplement to Hα imagery in diagnosing flares. Section 8 ends with a discussion of our conclusions from the study.

## 2. IMAGE TIME FLARE PROBABILITY DIAGNOSIS METHOD 1

After acquiring the new ISOON Hα image sequences and partitioning them into the ISS as listed in Table 1, we tried them out on the legacy flare probability diagnosis development and application algorithms from the previous study. Norquist and Balasubramaniam [1] refer to this version as the Hα Eigenvector Flare Categorization (HEFC) algorithms. In this report we will refer to it as the Image Time Flare Probability Diagnosis Method 1. See Norquist and Balasubramaniam [1] for a detailed description of the algorithm.

For our purposes in this report, we summarize the description as follows. The HEFC (hereafter, Method 1) development algorithm used the eigenvalues corresponding to each generated eigenvector to determine the number of eigenvectors to use as predictors. We used the number of eigenvectors corresponding to the greatest number of eigenvalues over all sequences in the development set that assured that 99.9% of the variance was explained in any sequence. This resulted in the use of the leading 25-50 eigenvectors depending on the development set used. The elements of the set of eigenvectors used were the predictor vector elements at each image time of the sequence.

Most of the experimentation with the flare diagnosis algorithms described by Norquist and Balasubramaniam [1] was focused on specifying the predictand at each image time. In this report we refer to the specified image time predictand as the "observed" flaring category. In the Method 1 development algorithm, we used the sub-region average Hα intensity of the date-active region from which the sequence data was taken to determine the image times of the flare rise. The prescribed non-zero flaring level indicator (FLI) for that image sequence was assigned as the predictand at those times, which were less than 10 percent of all image times in almost all FLI 1-3 sequences. At all other image times in the sequence and for all times in FLI 0 (non-flaring) image sequences, the predictand was set to zero. As mentioned in Section 1, a spike in the Hα eigenvectors coincident with x-ray flux rise assured that the flare had indeed occurred in the sub-region of the subject date-active region. Since we were using sub-region average Hα intensity in the HEFC algorithm, we verified that its rise coincided in time with the x-ray flux rise used with the eigenvector patterns to set the FLI. In the development algorithm, we checked the flare peak x-ray flux, and maintained zero predictands in the flare rise if it was less than the background value computed from the prior day's x-ray flux time series. Background x-ray flux was determined using the NOAA Space Weather Prediction Center "X-ray Bkgd Flux" method (see http://www.swpc.noaa.gov/wwire.html).

This process of setting the predictor vector and predictand for each image time was repeated for all image sequences in the development set. All such specified predictor vector-predictand pairs for all image sequences in the development set were input into the MVDA routine, which was Fisher's Linear Discriminant for Multiple Groups (see Appendix B of Norquist and Balasubramaniam [1], or Wilks [3]). Here, the "groups" are the four FLI categories. The MVDA routine produced discriminant vectors with the same number of elements as the predictor vectors.

3

For the four-group MVDA, there were three discriminant vectors, and four group-mean vectors whose elements were the means of the eigenvector elements over all predictor vectors associated with each flare category. The dot product of each discriminant vector with each group mean vector determines the component in 3-D discriminant space of the location of the group mean. The last step in the Method 1 development algorithm was to apply the discriminant vectors to each of the predictor vectors that were used in the MVDA routine. This also "places" the corresponding image time in discriminant space. Its distance from each of the four group means determines the probability of the four FLI categories, with the closest one being the group with the largest probability. The four probabilities sum to one, with each indicating its likelihood of occurrence. By comparing these probabilities with the prescribed FLI category, we got a preliminary look at how well the scheme was able to discriminate among the flaring categories.

The Method 1 application algorithm ingested the discriminant vectors and group mean vectors from the development algorithm. It also input the leading (same number as used in the development algorithm) eigenvector elements for each image time of each image sequence of the designated application set as the predictor vector elements. In this study period, we used a combination of two of the ISS from Table 1 as the development set and the other image sequence set as the application set. The discriminant vectors were dotted with each application set predictor vector, and the resulting location in discriminant space was compared with the four group mean locations to determine the probabilities of the four flaring categories.

## 3. IMAGE TIME FLARE PROBABILITY DIAGNOSIS METHOD 2

A look at some preliminary results from the Method 1 algorithms (not shown) indicated some degree of overlap among the four groups. At many FLI 0 image times in an application sequence, one of the non-zero FLI categories was diagnosed with the largest probability. This was often due to none of the four categories having a probability exceeding 0.5, leading to an ambiguity in the designation of most likely flaring category. We felt that this suggested a need to achieve greater separation among the group means in discriminant space to get a more distinctive diagnosis of flare category probability.

In seeking greater discrimination among the flaring categories, we experimented with using alternative forms of the eigenvectors. We saw that the range of values for a specific eigenvector would vary from sequence to sequence. Since we were using multiple image sequences in the development algorithm, we sought a more uniform representation of the eigenvector information across sequences. To that end, we considered the use of the time rate of change of the eigenvectors instead of their actual value at each image time. Since the image cadence is one minute for the ISOON Hα images, we decided to examine the use of 1-minute eigenvector changes as the predictors.

We then applied a five-point smoother to the time series of each of the nine leading eigenvectors, then created a scatter plot of one-minute eigenvector changes against one-minute x-ray flux changes for each eigenvector of selected image sequences with FLI categories 0-3. Examples are shown in Figure 1 for each of the four FLI categories.
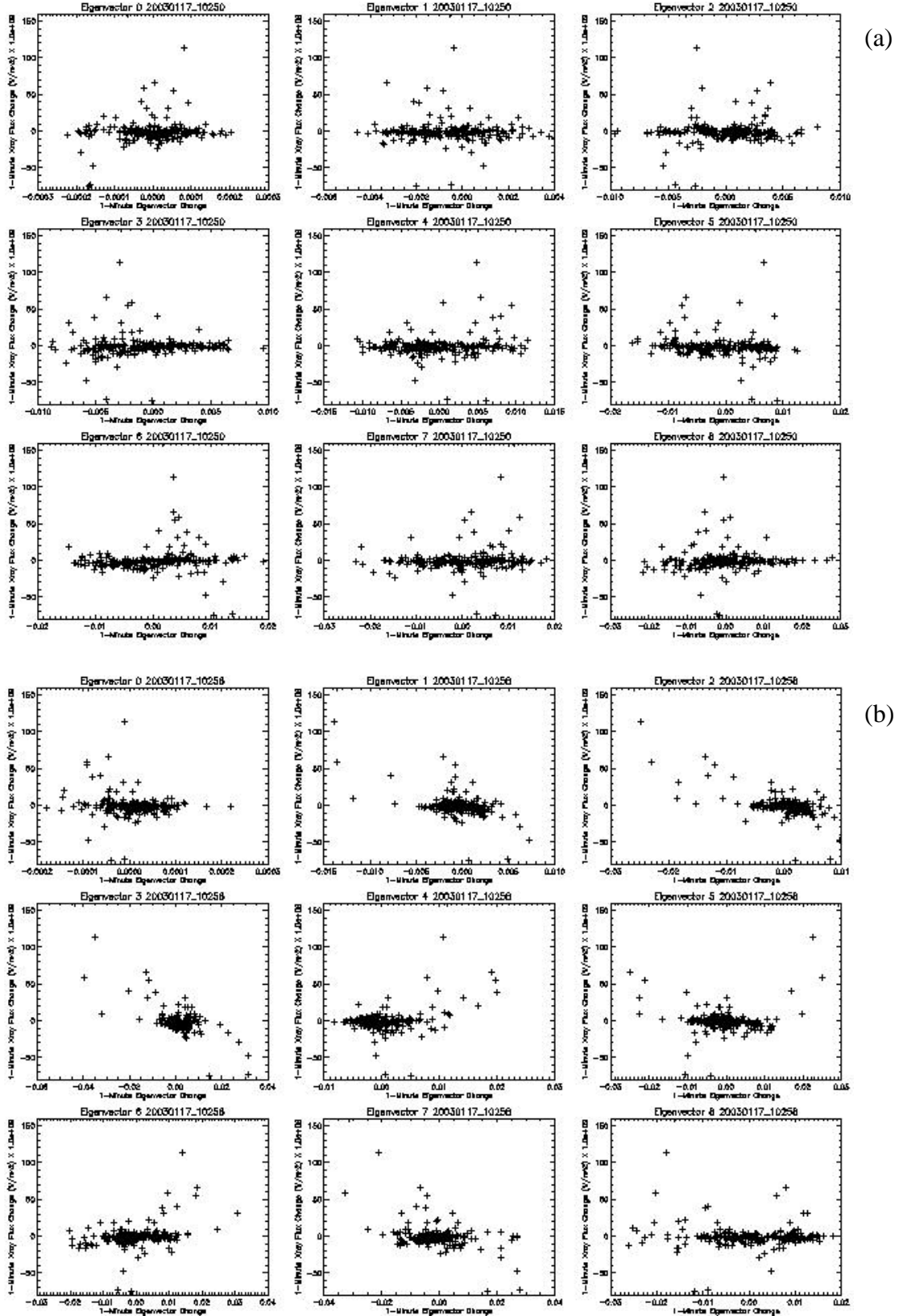
**Figure 1. X-ray Flux vs. Eigenvector Change for FLI (a) 0, (b) 1, (c) 2, and (d) 3 Sequences**
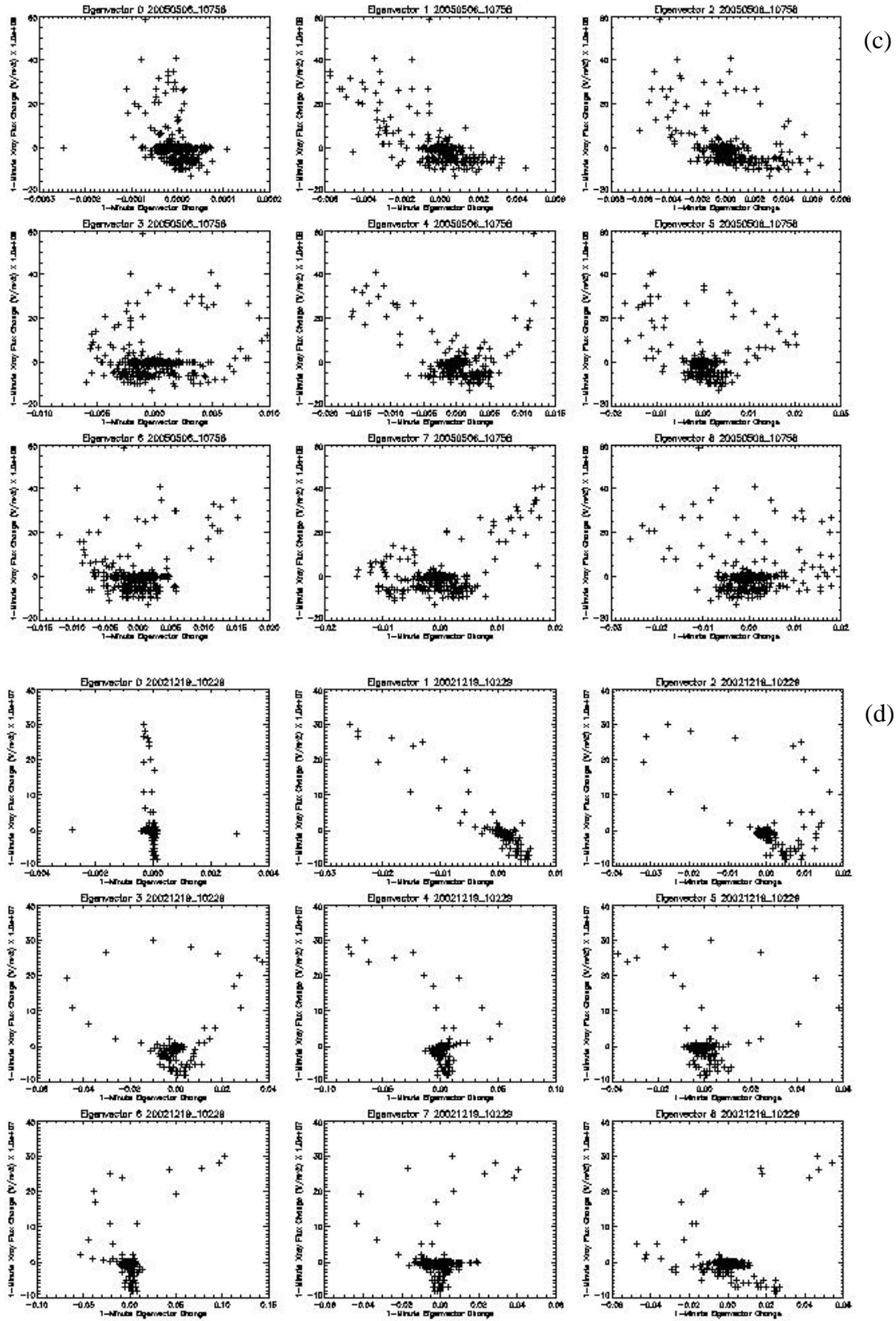
5

(c)

(d)

**Figure 1. (Cont.)**

From the scatter plots, it is clear that inflections (that is, large one-minute changes) in certain eigenvectors were coincident with large rises (that is, positive changes) in x-ray flux. In some cases (especially FLI 1) the sign of the large eigenvector changes was significant – in others (FLI 2,3) both signs were evident in the large changes. From this, we concluded that using one-minute changes in the leading eigenvectors as predictors and prescribed FLI predictands assigned during x-ray flux (not area-average Hα) rise times might enhance the discrimination among flaring categories.

To implement this idea, we made the following changes to the Method 1 development algorithm:
- Eliminate use of eigenvalues to determine the number of eigenvectors used as predictors;
- Impose use of a pre-set number of leading eigenvectors – initially eigenvectors 0-9;
- Change from eigenvector values to one-minute changes of smoothed eigenvectors as predictors;
- Eliminate use of sub-region area-average Hα intensity to indicate times of flare rise;
- Set prescribed non-zero FLI as predictands at x-ray flare rise times coincident with eigenvector inflections;
- Predictor vector-predictand pair exists at all image times for which the image time one minute prior is available.

As with Method 1, the x-ray rise times constituted less than 10 percent of all image times in almost all FLI 1-3 sequences. In the modified application algorithm, we also used as the predictor vector elements the pre-set number of leading eigenvectors at all image times in each application sequence in which the one-minute change of the smoothed eigenvectors was available. The application algorithm computed the dot product of the discriminant vectors derived in the development algorithm and each predictor vector, resulting in the location of the discriminant function value for each image time in discriminant space. It then computed the application probability of each flare category its distance from each of the four group mean locations in discriminant space. We designated the resulting development and application algorithms the Image Time Flare Probability Diagnosis Method 2.

## 4. ASSESSMENT OF FLARE PROBABILITY DIAGNOSIS METHODS 1, 2

Both Method 1 and 2 produce a diagnosis of the probability of the four flare categories at each image time of an image sequence. In this section we describe statistical metrics used to assess the performance of the two individual image time flare probability diagnosis methods, and present results from this assessment.

We computed a probability-weighted diagnosed flaring category $C_p$ given by

$$C_{p_i} = \sum_{g=0}^{G-1} g p_{g_i} \qquad [1]$$

at each image time $i$, where in our study there are $G = 4$ groups $g = 0, 1, 2,$ and $3$, and $p_g$ is the diagnosed group probability. From $C_p$ and $C_o$, the observed category at each image time $i$, several statistical metrics were determined for the image sequence. They are Brier Score

$$BS = \frac{1}{N(G-1)^2} \sum_{i=1}^{N} (C_{p_i} - C_{o_i})^2, \qquad [2]$$

7

Bias

$$Bias = \frac{1}{N(G-1)} \sum_{i=1}^{N} (C_{p_i} - C_{o_i})$$  [3]

and Diagnosis Uncertainty

$$DU = \frac{1}{N} \sum_{i=1}^{N} [1 - \max_g (p_{g_i})].$$  [4]

In our study, $N$ represents the number of image times in the respective image sequence. In addition, frequency distribution fit (FDF) defined by

$$FDF = \frac{1}{N_a} \sum_{g=0}^{G-1} \left| \frac{m_g}{n_g} - 1 \right| n_g$$  [5]

was computed over all image times in all application set sequences ($N_a$), where $m_g$ is the number of image times in which group $g$ was the most likely category (greatest diagnosed probability), and $n_g$ is the number of observed group $g$ image times.

We executed the development algorithm of Image Time Flare Probability Diagnosis Methods 1 and 2 using successive pairs of the three ISS listed in Table 1. We then applied the resulting discriminant vectors to the third (independent) image sequence set in the corresponding application algorithm. This yielded separate values of the statistical metrics for each of the three application sets by image sequence and overall. In the following illustrations of the results, we show the results from Methods 1 and 2 in direct comparison for each application set.

In Figure 2, we show Brier Score results from the two methods for all three application sets. In the plots, "D/A" stands for "Diagnosis/Application." We consider Brier Score to be the best single indicator of the performance of the flare category probability diagnosis techniques. It measures the mean squared difference between the probability-weighted diagnosed flare category (PWDFC) and the observed flare category. A perfect diagnosis of the flare category at all image times would yield a Brier Score of 0. Brier Score increases as the average difference between PWDFC and observed category over the image times in a sequence gets larger, with a maximum (worst) value of 1. Because all four categories generally have a non-zero probability, the PWDFC tend to stay between 0.5 and 2.5 so that we would never expect either a perfect or worst Brier Score.

In the results shown in Figure 2, the D/A Method 1 appears to perform somewhat better for most image sequences in Application Sets 1 and 3, but Method 2 is clearly better in Application Set 2. The two methods most closely correspond to each other in Application Set 2. Interestingly, the largest Brier Score values were for the image sequences from 20030117 in all three application sets. Norquist and Balasubramaniam [1] found that Method 1 and earlier flare category probability diagnosis algorithms tended to perform worst on prescribed FLI 0 sequences. They diagnosed the largest probability for a non-zero FLI category in an excessive number of image
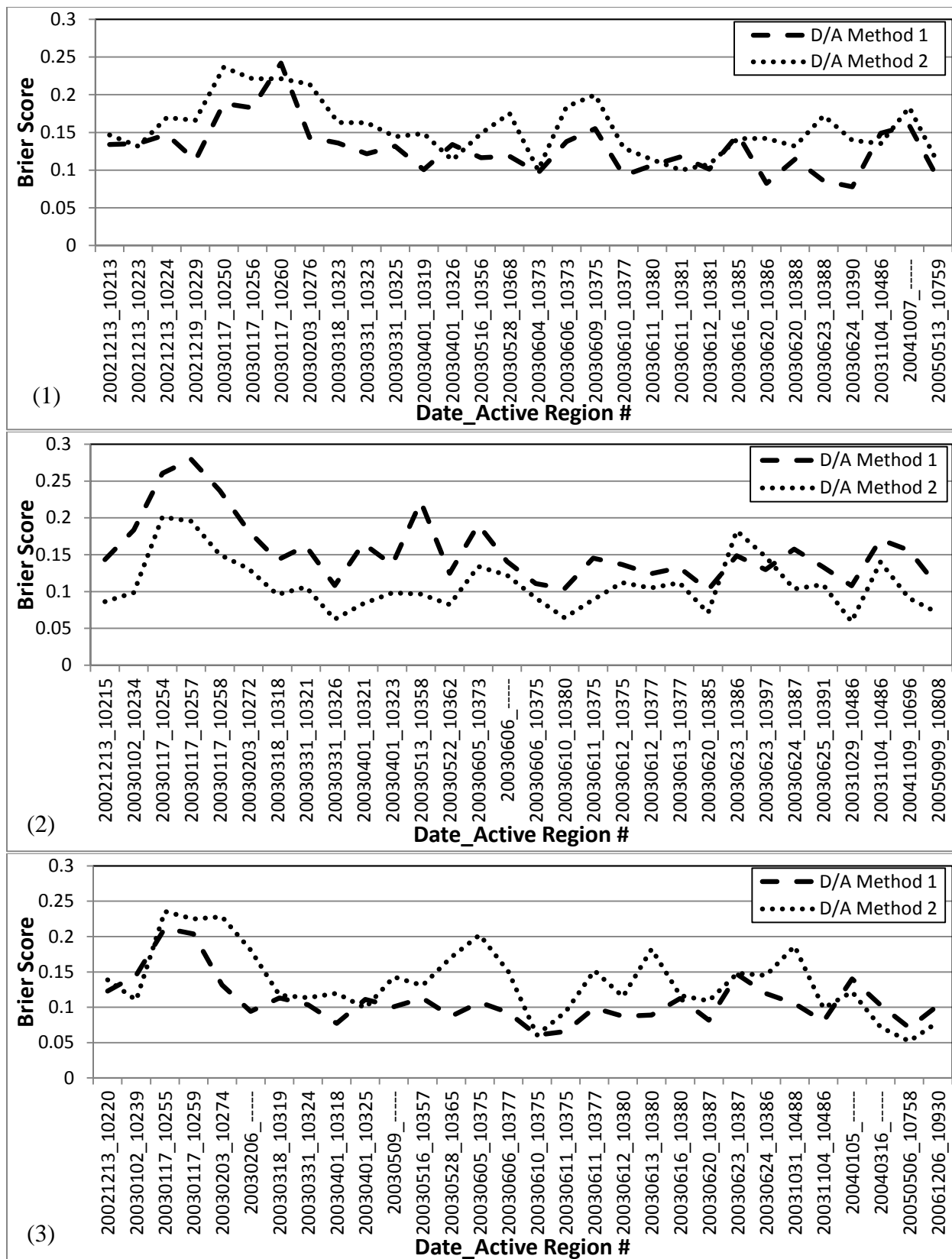
**Figure 2. Brier Score of Methods 1 and 2 for Application Sets (1), (2) and (3)**

9

times. In this study, we did not find that to be true – that is, poor Brier Scores were not exclusive to the FLI 0 sequences, and many FLI 0 sequences had quite good Brier Scores. For example, Application Set 1 image sequences 20030117_10250 and 20030604_10373 had Brier Scores of 0.19 and 0.10 respectively from Method 1, yet they were both prescribed FLI 0 sequences. This was also true of the FLI 0 sequences 20030605_10375 (BS of 0.20) and 20030610_10375 (BS of 0.06) from Method 2 in Application Set 3. Similarly, there was no definite association between the Brier Score and percentage of non-zero FLI image times in the flaring sequences. Brier Scores seemed to be insensitive to the number of observed flaring times in the image sequence.

Figure 3 shows the Bias from the two development/application methods. It shows very nearly the same patterns as Figure 2 for Brier Score, primarily because the diagnosis methods systematically diagnose a PWDFC larger than the observed category at the image times. If there were offsetting diagnoses of positive and negative PWDFC-minus-observed FLI, the Bias would have a different pattern from sequence to sequence than the Brier Score. However, we know that can't happen because as was mentioned earlier, the PWDFC generally ranges between 0.5 and 2.5, and the observed FLI (OFLI) at image times are dominated by zeros. Therefore, there is an inherent positive value to the Bias metric. To get an idea of the lower limit of Bias for a prescribed FLI 0 image sequence, we start by noting that an image time probability diagnosis of 0.85, 0.05, 0.05, and 0.05 for FLI 0-3 respectively corresponds to PWDFC = 0.3. If this diagnosis were made at all image times in the sequence, a Bias of 0.10 would result. This would seem to be an approximate lower limit to the Bias for image sequences. More realistically, at least for Methods 1 and 2, a diagnosis of 0.70, 0.15, 0.10, and 0.05 would likely be the best that could be achieved, giving a PWDFC = 0.5. If repeated at all image times in the sequence, a Bias of about 0.17 would result, considered a "best" Bias for a prescribed FLI 0 sequence processed by these methods.

In sequences where the number of OFLI 0 was grossly under-represented by the probability diagnosis (that is, where the diagnosed most likely category, DFLI, was > 0 at most image times), an excessive number of false alarms were indicated. For example, the FLI 0 image sequence 20030117_10257 with a bias of 0.51 had only 70 of 216 image times with DFLI 0 in Method 1. The other image times had DFLI of 1-3, which of course would be considered false alarms. By contrast, in Method 2 the FLI 0 sequence 20030620_10385 had a bias of 0.19 with 306 of 393 image times with DFLI 0, resulting in a much smaller false alarm rate.

The disparity of flare category probability diagnosis performance among ISOON image sequence begs the question "why are some sequences diagnosed so much better than others?" While it is outside the scope of this report to investigate this matter thoroughly, we can at least look at a couple of sequences with contrasting performance to suggest an answer. In Figure 4(a) we show the leading nine eigenvectors for the FLI 0 image sequence 20030117_10250, while in Figure 4(b) we show the PWDFC at all image times resulting from the Method 2 probability diagnosis (Bias = 0.48) based on those eigenvectors. We show the same pair of plots for the FLI 0 sequence 20030620_10385 in Figures 5(a) and (b) respectively using the Method 2 probability diagnosis (Bias = 0.19). Figure 4(a) for FLI 0 sequence 20030117_10250 depicts the smooth, sinusoidal pattern commonly associated with FLI 0 sequences. However, the resulting Method 2 PWDFC in Figure 4(b) hovers around 1.5 suggesting that the discriminant vectors for development set 2_3 in this case are placing the discriminant functions evaluated from those
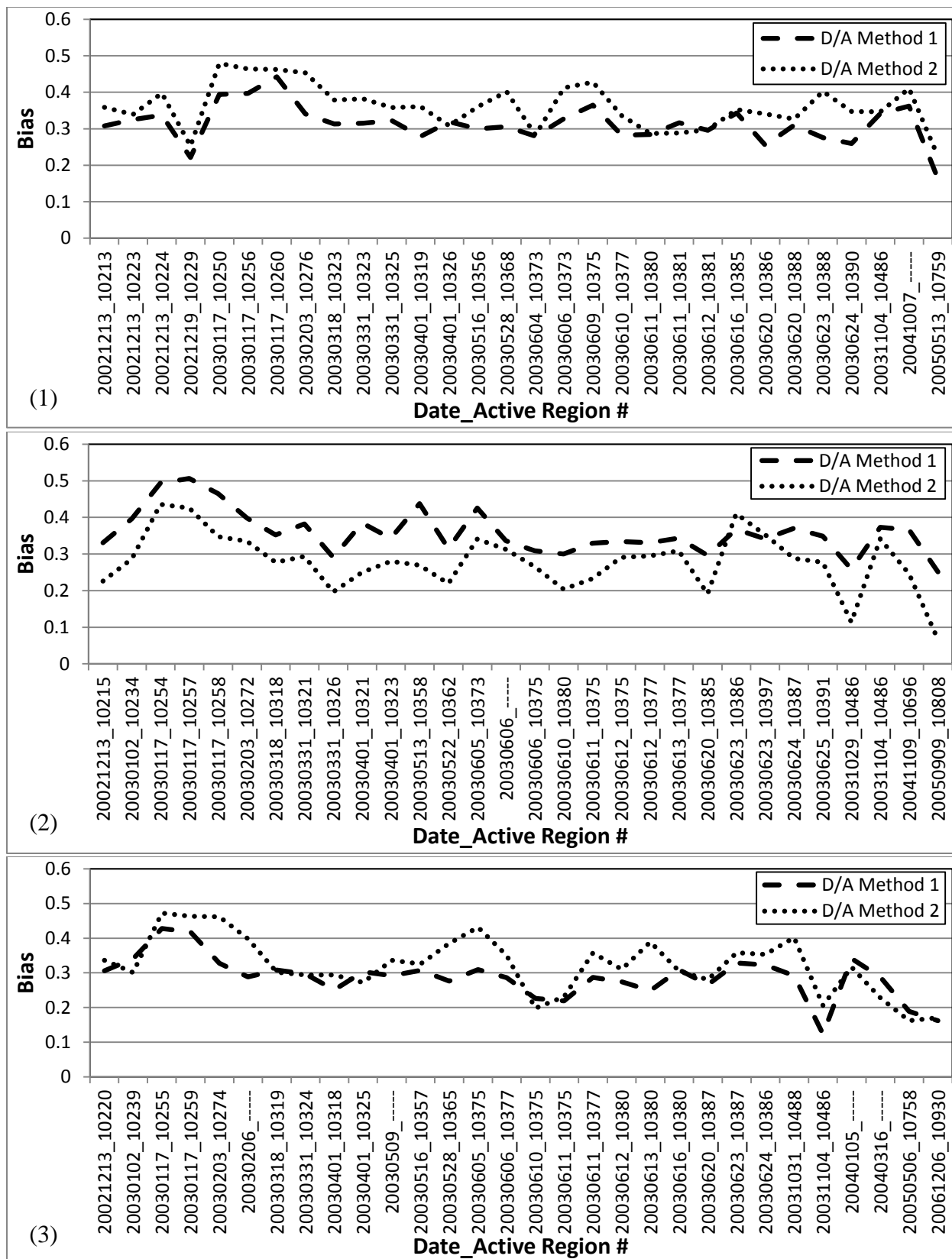
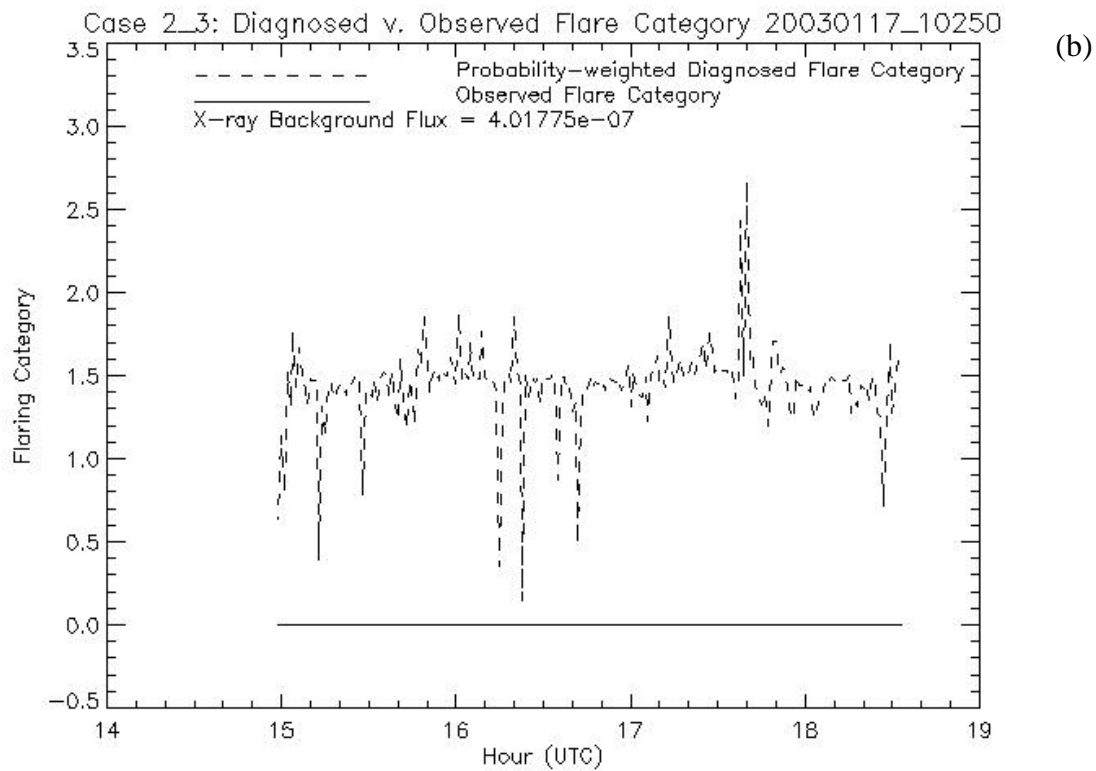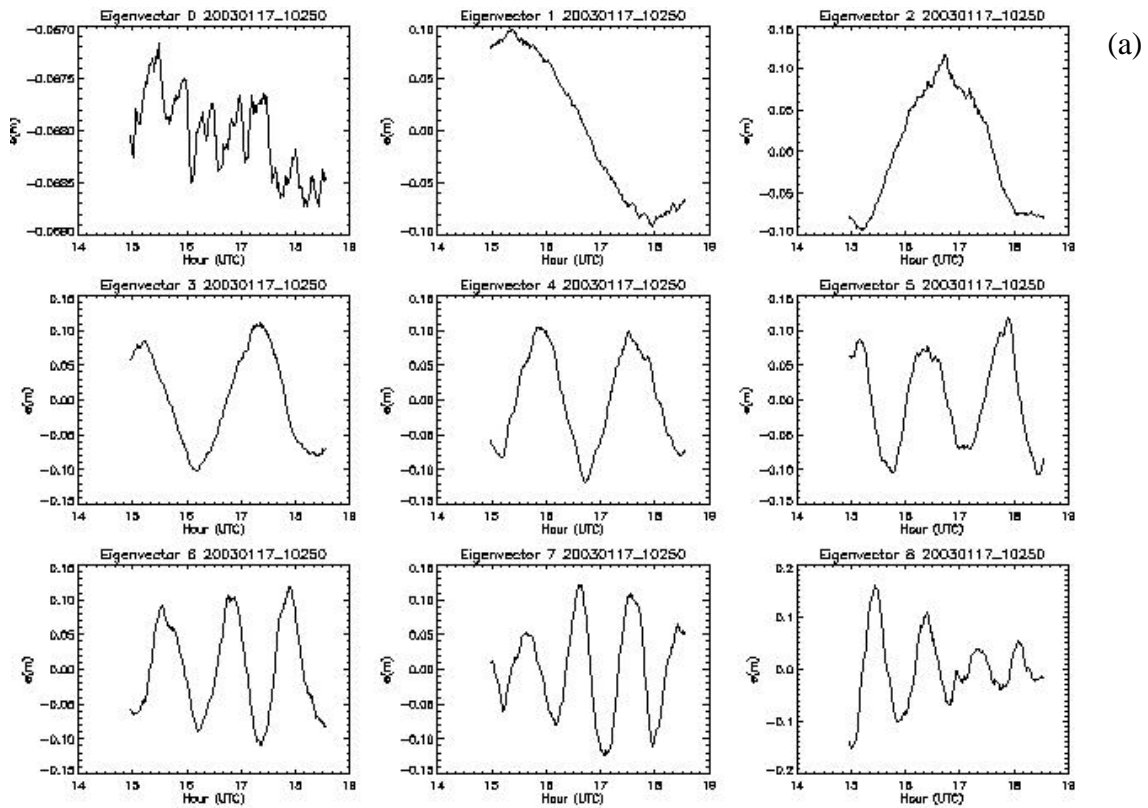**Figure 3. Same as in Figure 2 Except for Bias**

**Figure 4. Sequence 20030117_10250 (a) 1st 9 Eigenvectors, (b) Method 2 PWDFC vs OFLI**
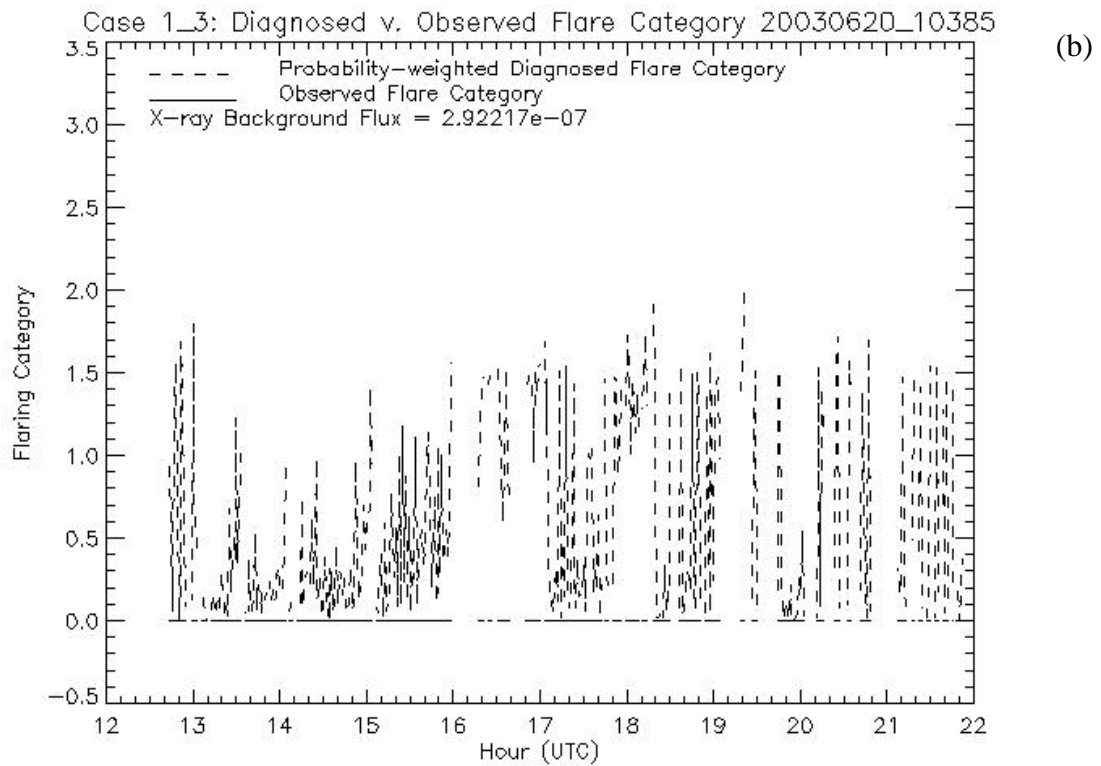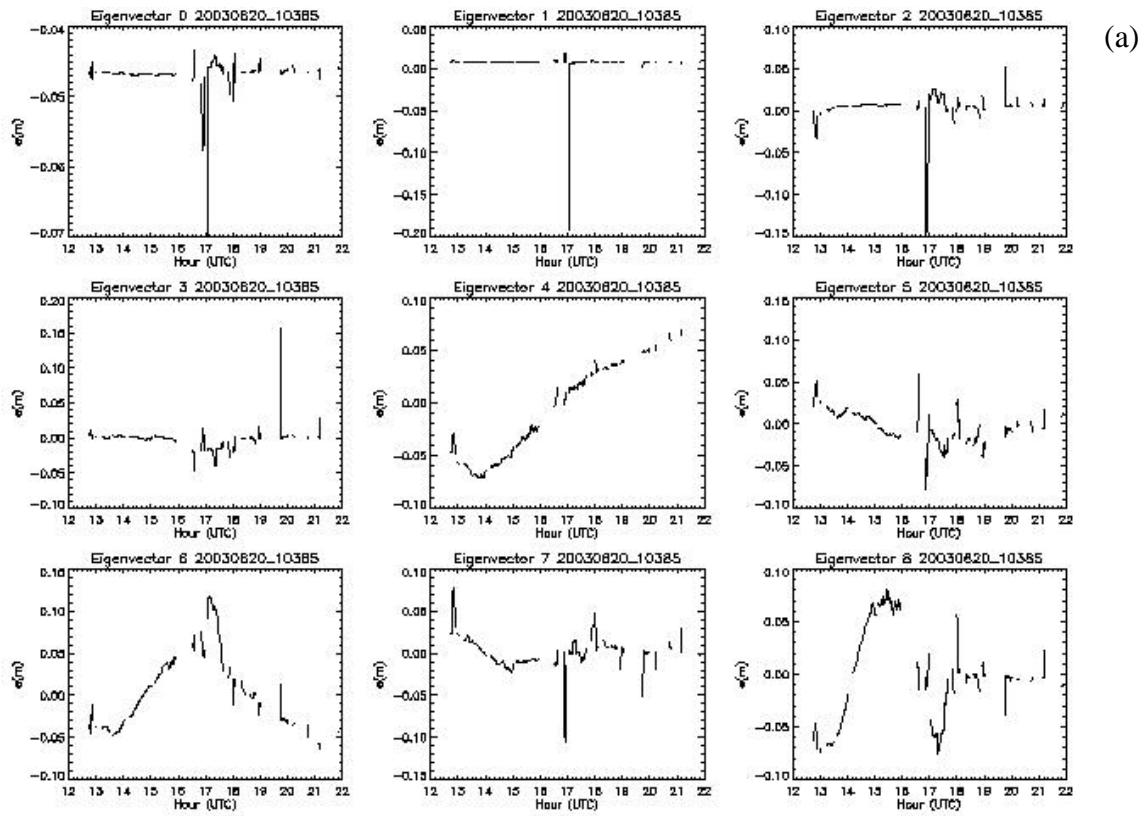
(a)

(b)

**Figure 5. Same as in Figure 4 Except for Image Sequence 20030620_10385**

eigenvectors closer to groups 1 and 2 (weak to moderate flaring) than to group 0 (non-flaring). The leading eigenvectors shown in Figure 5(a) for FLI 0 sequence 20030620_10385 are strikingly different than in Figure 4(a) – flat with occasional spikes, with only a hint of sinusoidal variation in eigenvectors 6 and 8. Figure 5(b) shows that the resulting probability diagnosis clearly favors group 0, and in fact resulting in quite high probability of the non-flaring category (not shown) at most of the image times. We can't draw any hard and fast conclusions from two cases, but there does seem to be a great deal of sensitivity in the diagnosis performance to the patterns of the eigenvectors. This pair of cases highlights the great variations of these patterns associated with a single flaring category. As such, it suggests that the limited discrimination among the flaring categories may be due to a lack of distinction among the eigenvector patterns of the image sequences of a particular prescribed FLI category when used in development. This would increase the in-group scatter in discriminant space and lead to less distinction among the groups.

We also show some results for FLI 1-3 image sequences from image time flare category diagnosis Method 2 in Figures 6-9. The leading nine smoothed eigenvectors (Figure 6(a)) and the diagnosed PWDFC vs. OFLI (Figure 6(b)) are shown for the image sequence 20030522_10362. The diagnosis yielded a Brier Score of 0.082 for this FLI 1 sequence. A C-class flare occurred between 20 and 22 UTC that is evident as inflections in several of the leading eigenvectors. The plot of PWDFC in Figure 6(b) shows quite a bit of variation during the sequence, but tends to remain around 0.5 except for several jumps to 1.5 or so. The same plots are shown for another FLI 1 sequence, 20030528_10368, in Figure 7. This case had C-class flares between 14 and 15 UTC and between 20 and 21 UTC as shown in Figure 7(b). The corresponding inflections are evident in some of the leading eigenvectors in Figure 7(a). However, in this sequence the diagnosis of PWDFC is greater, staying above 1 at most of the image times. As a result, the Brier Score for this sequence was not as good, 0.175. In Figures 8 and 9, we show leading eigenvectors and Method 2 PWDFC vs. OFLI for the FLI 2 sequence 20050506_10758 (Brier Score 0.052) and the FLI 3 sequence 20050909_10808 (Brier Score 0.071). Both of these diagnoses represent the flare well. This is likely due to the prominent inflections in the leading eigenvectors and the characteristic eigenvector patterns representing these two FLI categories.

Figure 10 depicts the Diagnosis Uncertainty (DU) over the image sequences of the three application sets. DU is a measure of the collective probabilities of flaring categories not identified with the largest probability. It is the complement to the degree of certainty of the most probable category. It does not directly relate to PWDFC accuracy, like Brier Score. However, especially for Method 2 we see a strong similarity in the sequence-to-sequence variation of Brier Score (Figure 2) and DU (Figure 10). On the other hand, a difference between the displays of Brier Score and DU is that the distinction between Methods 1 and 2 in Application Set 3 for Brier Score is greater for DU. It appears that greater certainty of the most probable category is generally associated with category diagnosis accuracy. The levels of DU for both methods in all put perhaps Application Set 2 are disappointing. A good diagnosis would have a higher than 50 percent probability of the most probable category. We see in Figure 10 that in many sequences the average DU approaches or exceeds 50 percent. In only 6 of the 30 sequences in Application Set 2 does the DU get below 30 percent, or a most likely probability of 70 percent that we suggested earlier might be the best we could do for PWDFC in these methods across a sequence.

(a)

(b)

**Figure 6. Same as in Figure 4 Except for Image Sequence 20030522_10362**

15

(a)

(b)

**Figure 7. Same as in Figure 4 Except for Image Sequence 20030528_10368**
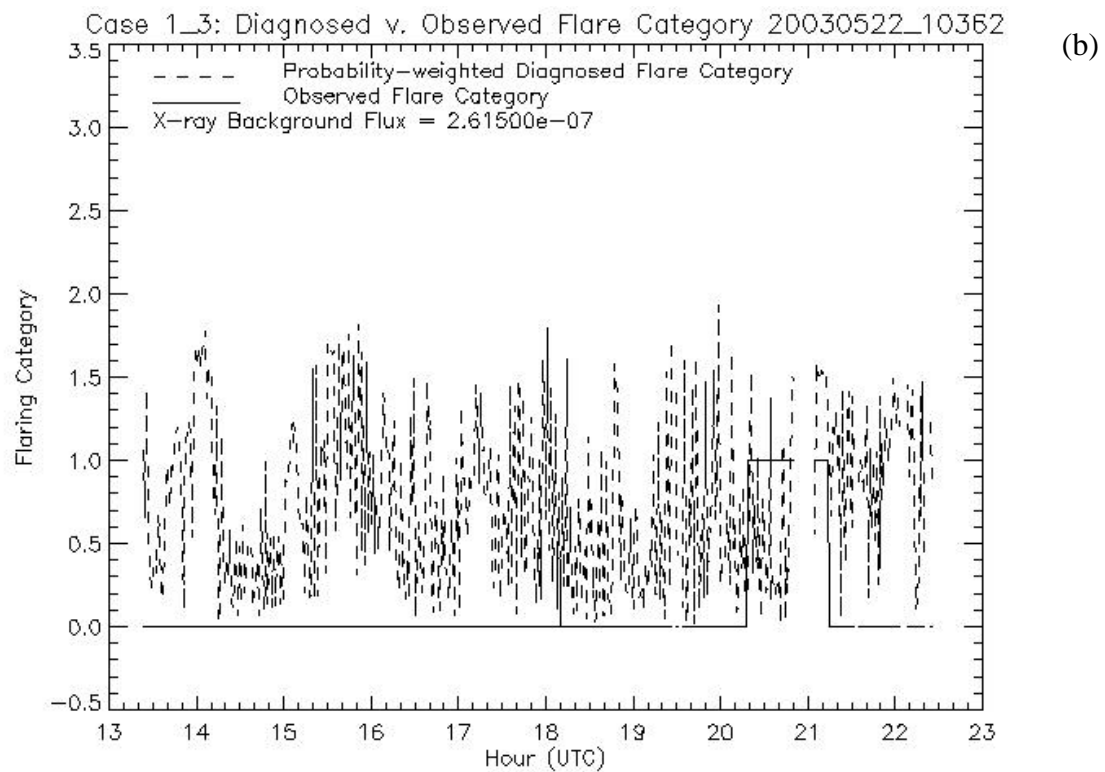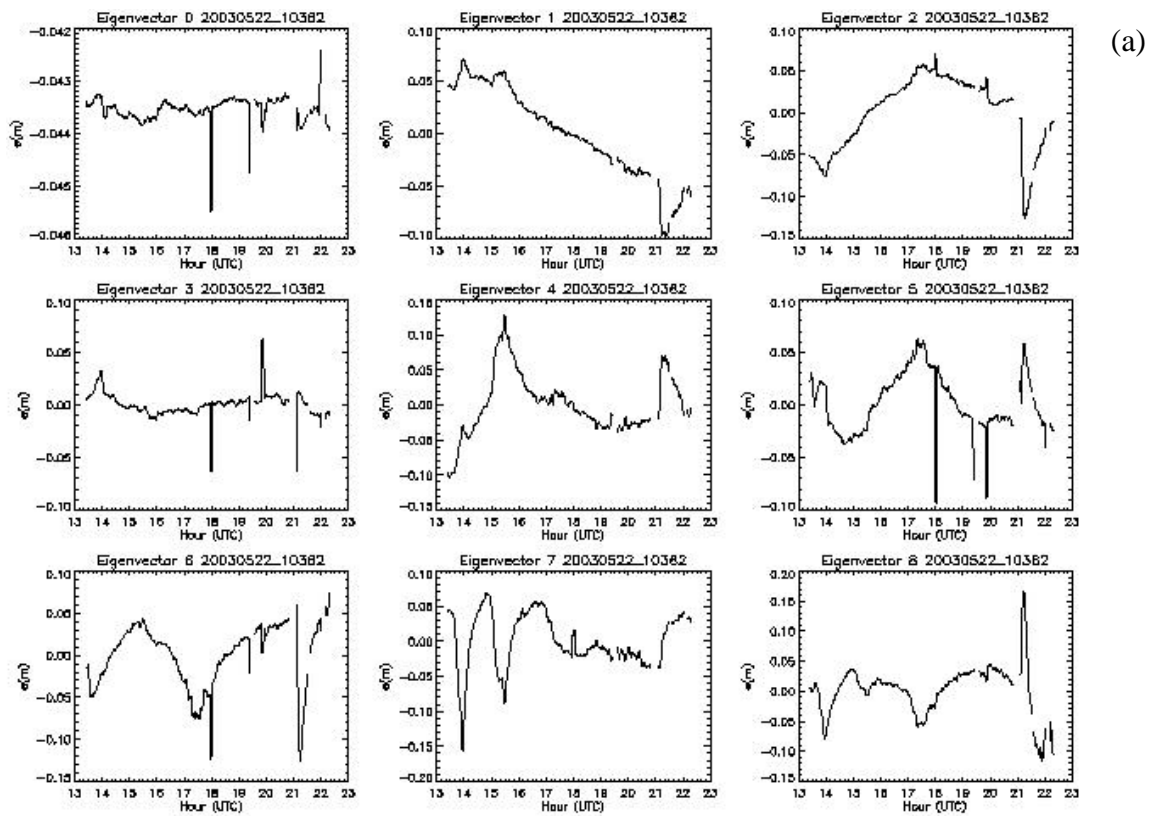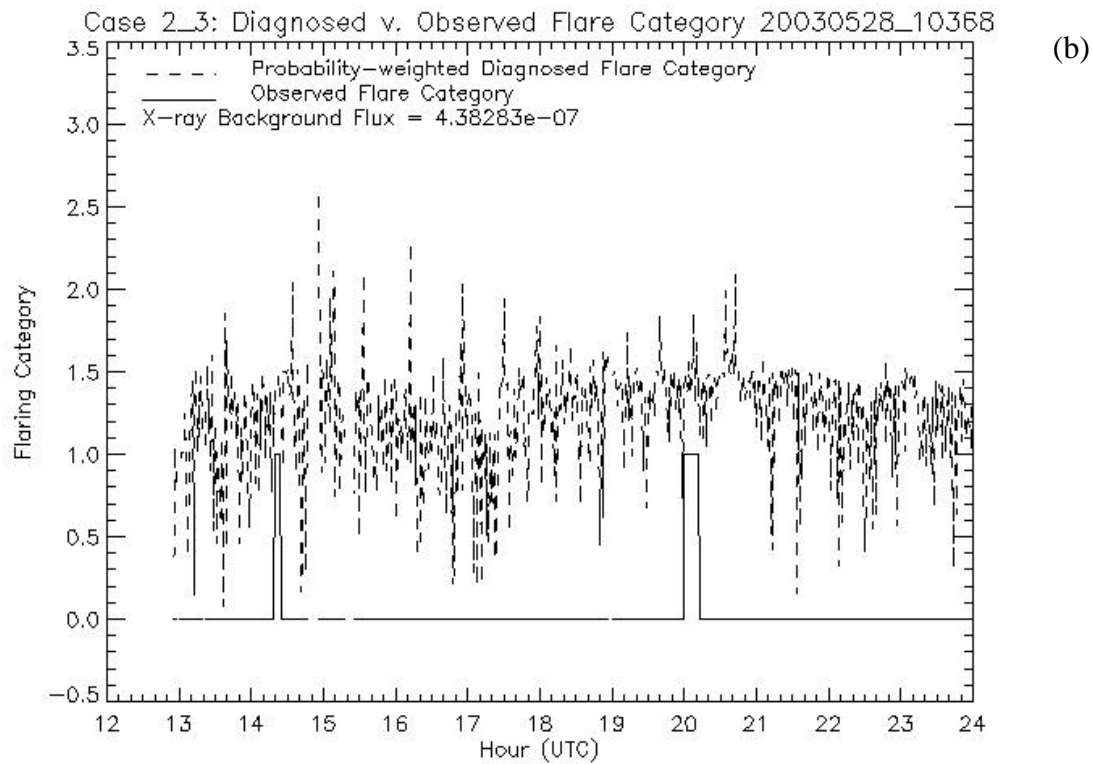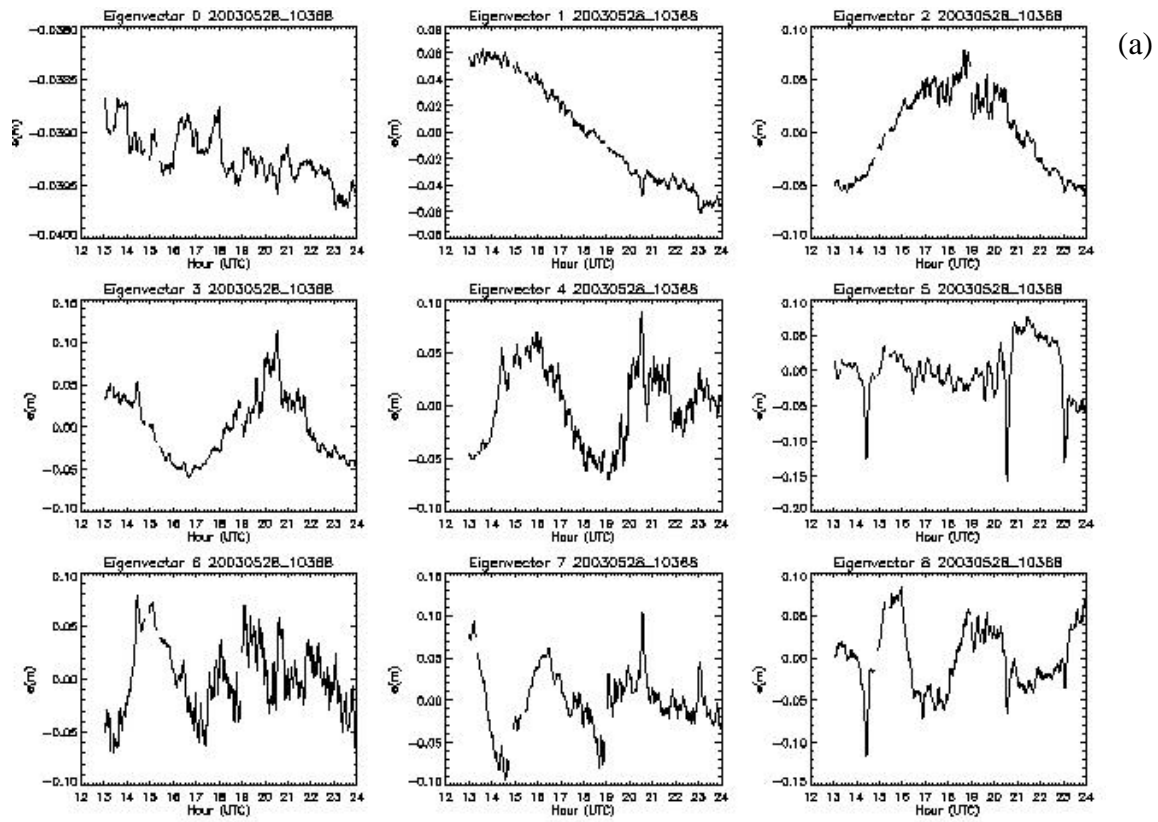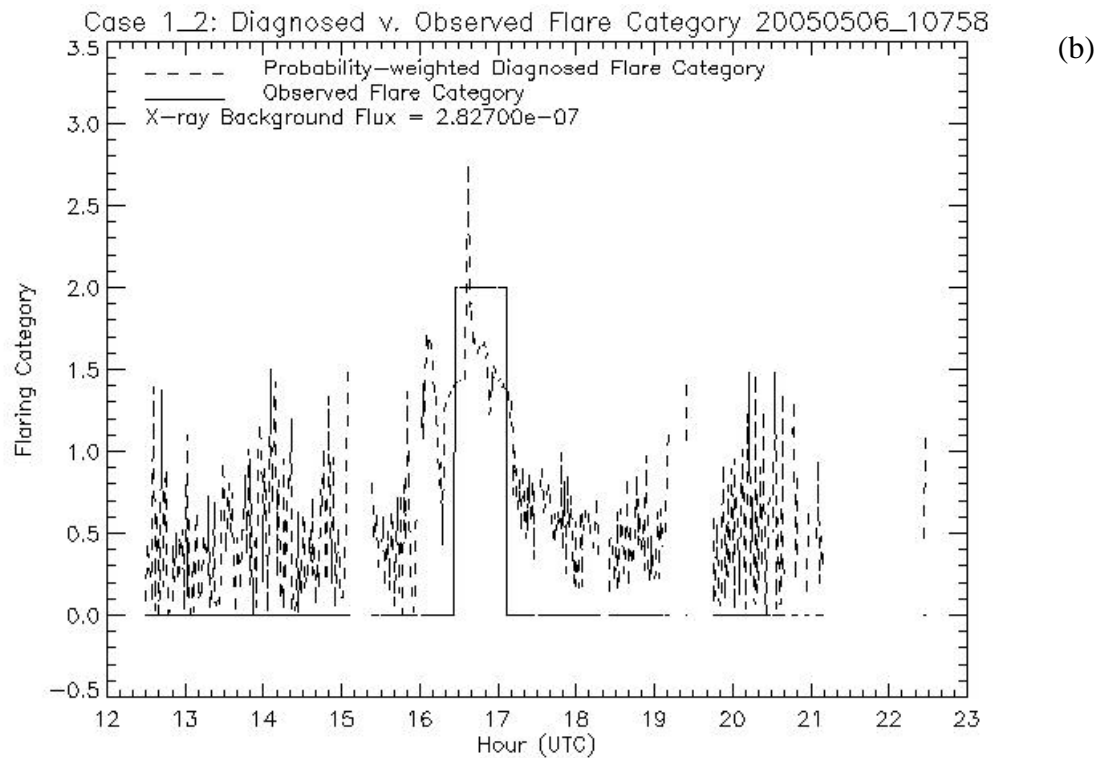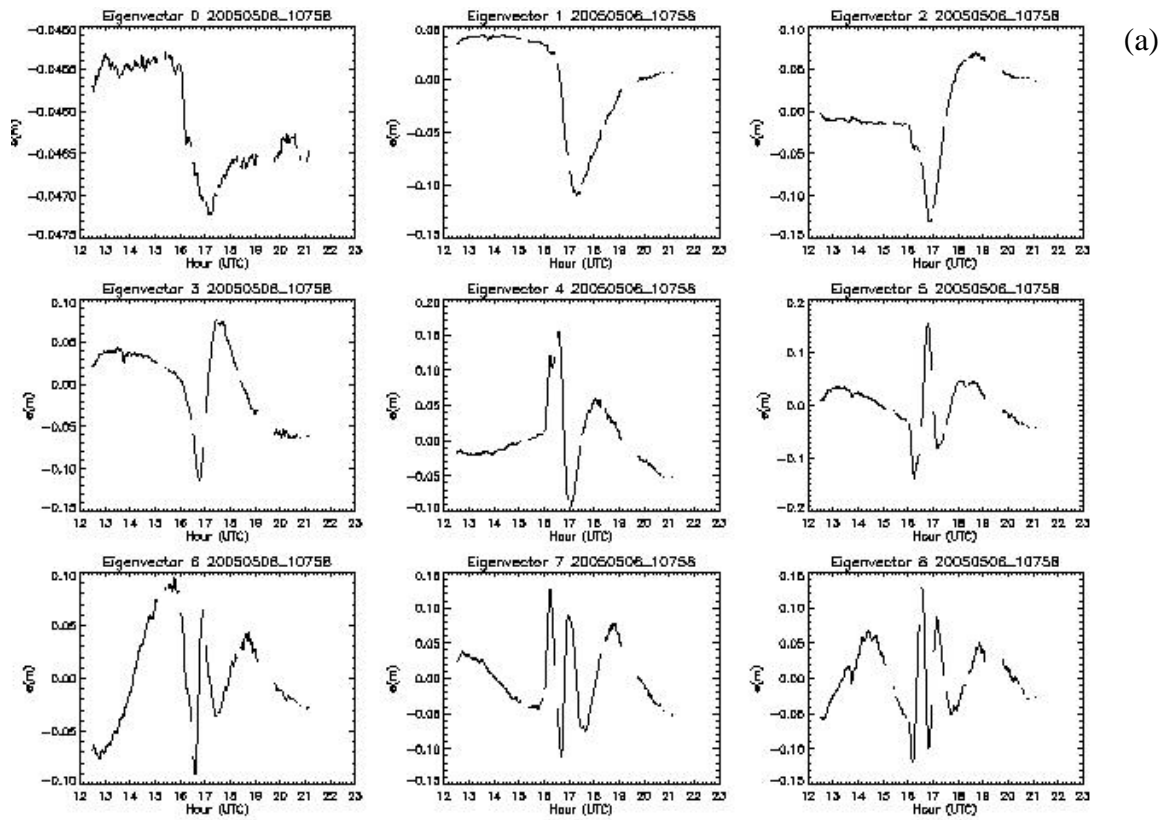
(a)

(b)

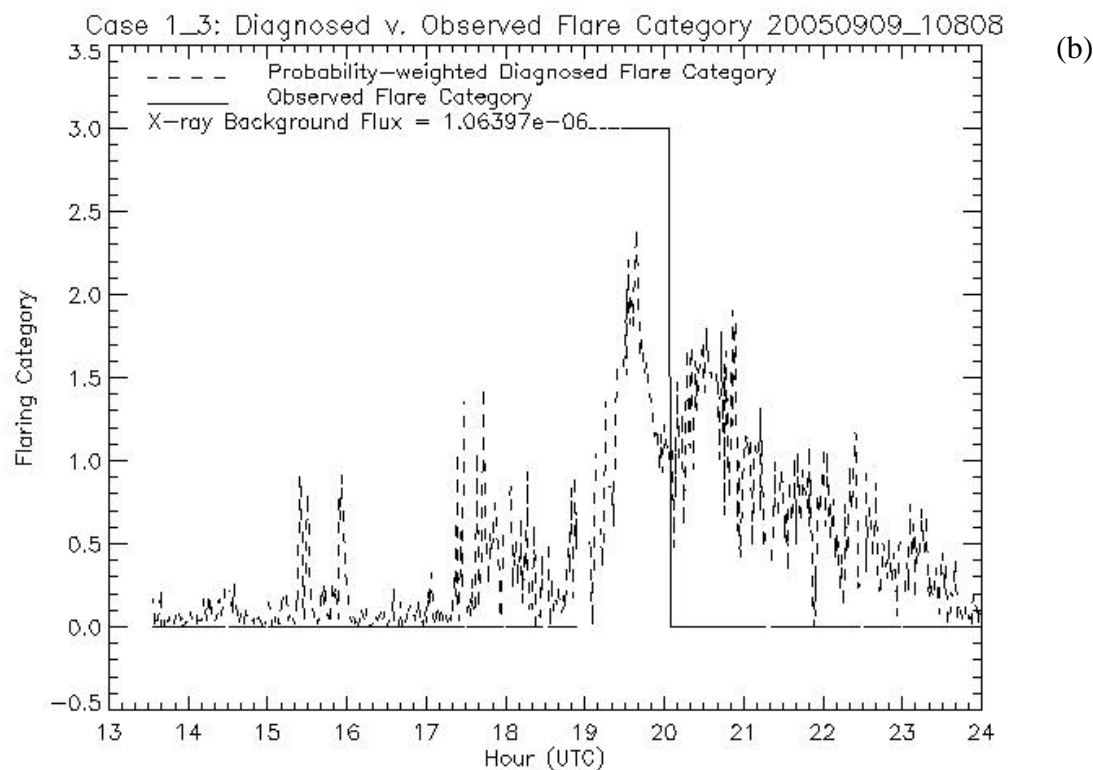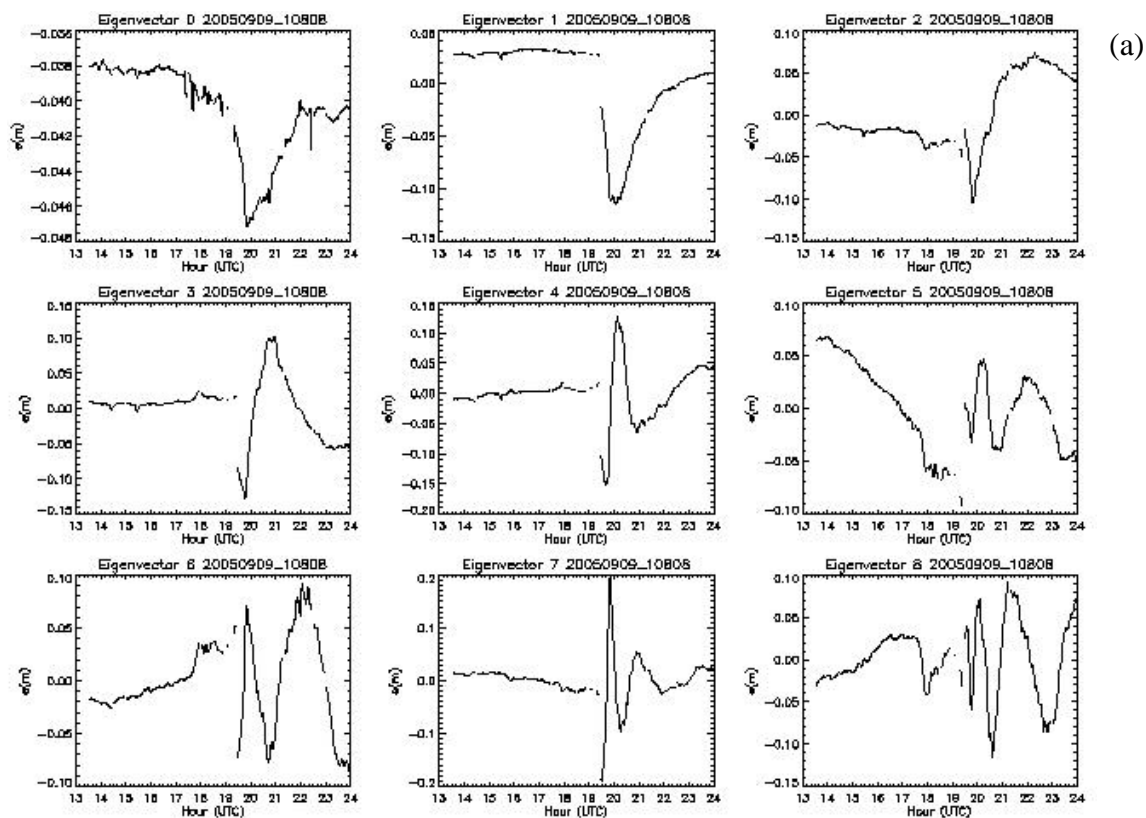**Figure 8. Same as in Figure 4 Except for Image Sequence 20050506_10758**

**Figure 9. Same as in Figure 4 Except for Image Sequence 20050909_10808**
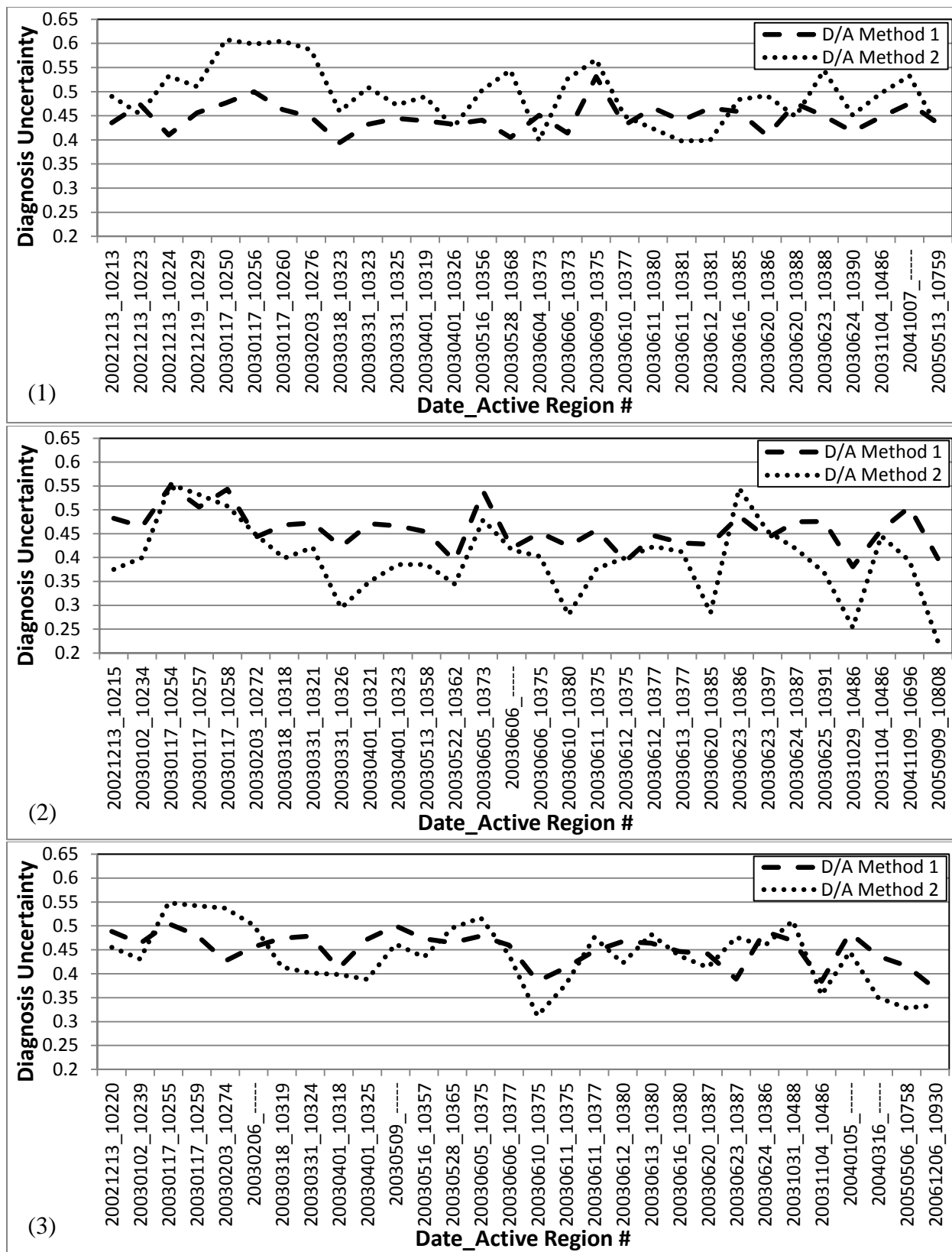
**Figure 10. Same as in Figure 2 Except for Diagnosis Uncertainty**

In addition to the statistical metrics computed for each image sequence as shown in Figures 2, 3 and 10, we present their values determined from all image times over all sequences in each application set in Table 2.

**Table 2. Methods 1, 2 Statistical Metrics for All Image Times in Each Application Set**

|  | Application Set 1 | | Application Set 2 | | Application Set 3 | |
|---|---|---|---|---|---|---|
|  | Method 1 | Method 2 | Method 1 | Method 2 | Method 1 | Method 2 |
| Brier Score | 0.12 | 0.15 | 0.15 | 0.10 | 0.10 | 0.13 |
| Bias | 0.31 | 0.35 | 0.35 | 0.27 | 0.28 | 0.31 |
| DU | 0.44 | 0.48 | 0.45 | 0.39 | 0.45 | 0.43 |
| FDF | 0.89 | 0.92 | 0.87 | 0.56 | 0.66 | 0.82 |

Method 2 performed the best overall on Application Set 2 (Development Set 1_3) followed by Method 1 on Application Set 3 (Development Set 1_2). Both methods varied in their diagnosis skill among the application sets, with Method 1 slightly better than Method 2 on Application Sets 1 and 3 and Method 2 somewhat better than Method 1 on Application Set 2. Based on these overall results, there is not a strong argument for one method over the other in flare category diagnosis performance. We would only recommend Method 2 in that it is simpler to implement, does not rely on area-average Hα intensity, and achieved the best overall performance.

# 5. WHOLE SEQUENCE ALGORITHM DEVELOPMENT/APPLICATION

In an attempt to improve the discrimination among flaring categories, we next took a radically different approach. Instead of trying to diagnose flare category for each individual image time as done to this point, we arrived at the idea of attempting to diagnose flare category for each sequence as a whole. The idea came from the observation that the leading eigenvectors did seem to fall into four distinct patterns as described above, with each pattern associated with a corresponding flaring level indicator (FLI). We decided to represent the distinct pattern numerically in the MVDA predictor vector elements for each sequence, and assign the FLI for that sequence as the predictand category. The representation was in the form of a frequency distribution of the 1-minute changes for each of the leading eigenvectors.

The frequency distributions were constructed for all 60 image sequences in each development set combination of ISS pairs. The $N_b$ 1-minute change bins were established separately for each of $N_e$ leading eigenvectors, resulting in $N_e \times N_b$ fractional frequency of occurrence values that were the predictors for each sequence. The predictand was the prescribed FLI value based on the eigenvector patterns and x-ray peak flux as done in the earlier methods. To set the size bins for each eigenvector, we sorted all of the 1-minute changes over all 60 sequences from largest negative to largest positive values. We then found the first and 99th percentile values, and used them to set outer bounds for the range of values. The outer bounds were set to the next integer value less than the first and greater than the 99th in the same power of 10. For example, if the first and 99th percentile values were -0.00467 and 0.00631 respectively, we set the outer bounds at -0.005 and 0.007 respectively. We then divided this range into $N_b$ equally sized bins. For each sequence, we counted the number of 1-minute changes that fell into each size bin corresponding to each of the $N_e$ eigenvectors, and divided each count by the total number of 1-minute changes

in the sequence. The resulting frequency of occurrence values for each of the leading $N_e$ eigenvectors made up the predictor vector elements for that sequence. In the same way, we computed the frequency of occurrence for the $N_b$ size bins for each eigenvector over all 60 sequences, separately by FLI category. The latter accounting was done simply to assess the overall differences in frequency distribution of the 1-minute changes by FLI category.

The 60 predictor vector – predictand sets were entered into the MVDA development algorithm to determine the three discriminant vectors of $N_e \times N_b$ elements. These were then applied back to the 60 predictor vectors used to develop them, just to test the MVDA algorithm process. The discriminant space position of the resulting discriminant function values for each FLI category was compared to the position of the four group means for each sequence, and the probability of each category was diagnosed. The result was perfect discrimination – the probability of the original FLI predictand value category was one, and the probabilities of the other three categories were zero. This is because each predictor vector to which the discriminant vector was applied was a predictor vector used to develop the discriminant vector, so the development and application steps were validated. We settled on the use of $N_e = 8$ leading eigenvectors and $N_b = 10$ size bins, resulting in 80 predictor elements used in the MVDA development algorithm.

We then applied the discriminant vectors derived from a particular development set of 60 image sequences to an application set of 30 independent image sequences. The three separate sets of 30 image sequences used in this report were listed in Table 1. For example, we derived discriminant vectors from development set 1_2, made up of 60 image sequence combined from sets 1 and 2, and applied them to application set 3. In the application algorithm, the predictor vectors are formed in the same way as described above, using the $N_e = 8$ leading eigenvectors and $N_b = 10$ size bins to develop the frequency of occurrence values for each sequence in the application set. The discriminant vectors from the development set are then applied to the predictor vector of each sequence in the application set. The position in discriminant space from the resulting discriminant function values is compared with the position of the development set discriminant function means of each category. The distance from each one determines the probability of each flare category. The closer the application diagnosis position is to one of the group means' position, the higher the probability and the lower the diagnosis uncertainty. However, if there is not a lot of distinction among the development set discriminant function means, there is a greater ambiguity in the application diagnosis, and the diagnosis uncertainty is greater. Thus, it is the goal of the multivariate discriminant analysis to maximize the separation among the group means, and to minimize the scatter of the development set discriminant function values within each group or category. The procedure will succeed or fail depending on these factors, so the trick is to design the predictors and predictands (that is, the categories) to optimize these factors.

We first assess the performance of the whole sequence development and application algorithms by looking at the probability-weighted diagnosis of flare category (PWDFC). Unlike the earlier methods that diagnose the probability of each FLI category and thus the PWDFC at each image time, here we determine PWDFC from the four category probabilities diagnosed for the entire image sequence. In Figure 11, we show the diagnosed PWDFC from the whole sequence method for all sequences in each of the three application sets. For reference, we also show the observed FLI (OFLI) for each sequence in each of the application sets. We see that the majority of the
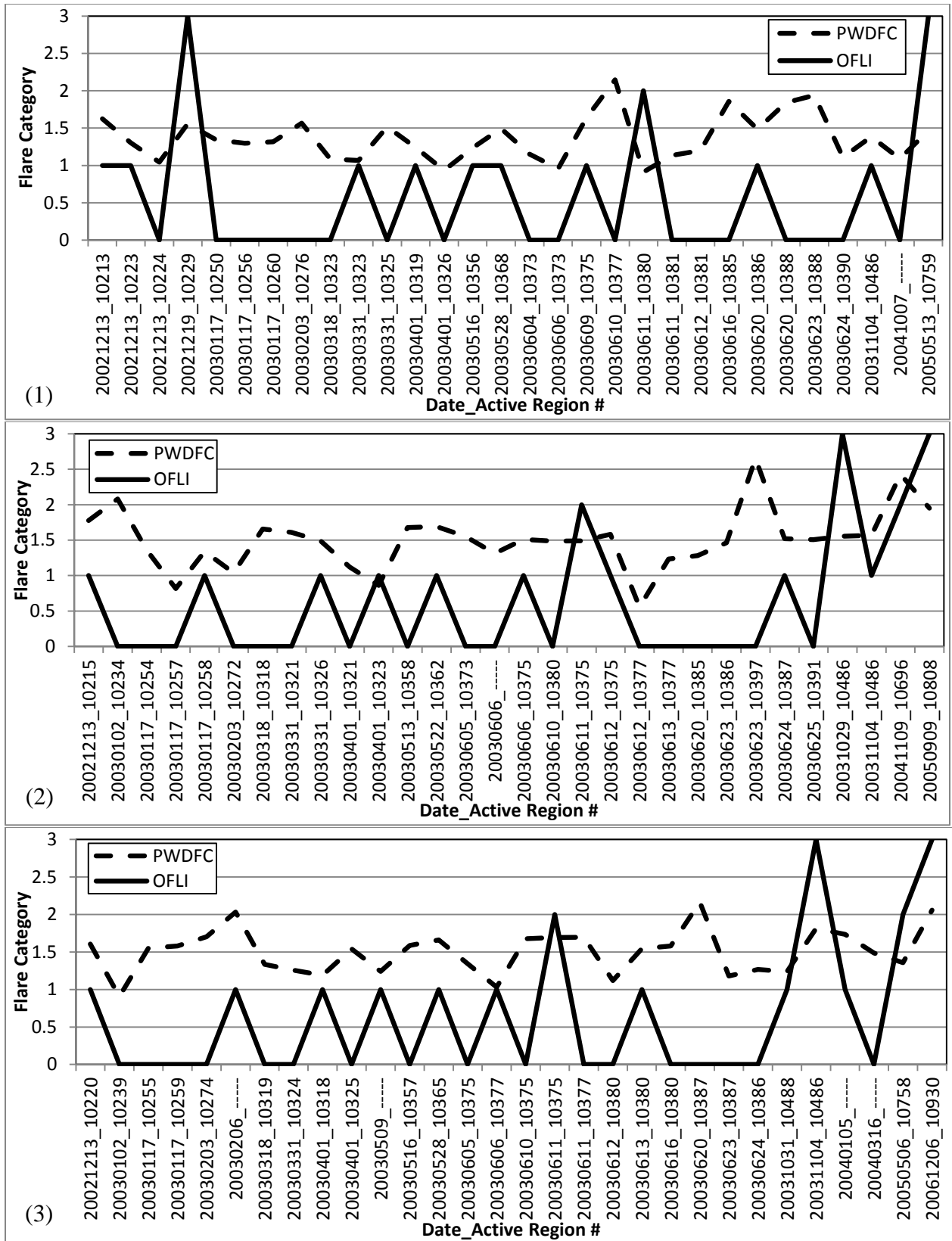
**Figure 11. Whole Sequence Method PWDFC vs. OFLI for Application Sets (1), (2), (3)**

sequences have diagnosed PWDFC between 1 and 2, with occasional diagnoses above or below this range. By contrast, OFLI flare categories 0 and 1 predominate in the sequences in all three application sets, with only a small minority of sequences having OFLI 2 or 3. Average PWDFC-OFLI difference for the three application sets were 0.8, 0.9, and 0.9 respectively. There does not appear to be any perceptible correspondence between the sequence-to-sequence variation of PWDFC and OFLI. For the 11 sequences with OFLI 2 or 3, only one (20041109_10696 in Application Set 2) had a corresponding rise in flare category to a comparable value.

We list the performance metrics results for the whole sequence development and application algorithms in Table 3. In this case, $N = 30$, the number of image sequences in each application set. The Brier Score and Bias are computed from the values shown in the PWDFC vs. OFLI plots in Figure 11. Recall that Brier Score and Bias are scaled to the range 0 to 1, so that that flare category bias is three times the Bias metrics in Table 3. The metrics indicate a consistency among the three separate application sets, implying the same for the development sets from which the application discriminant vectors were derived. Since the metrics here are computed over 30 sequences for each application set rather than thousands of individual image times as in the previous sections of this report, we can't make a direct comparison with the metrics values in Table 2. It is clear from Table 3 metrics that the whole sequence development/application algorithms produce a consistent positive flare category bias. This is indicated by both the Bias and the comparison of percentage of sequences with diagnosed FLI 0 (% DFLI 0) and observed FLI 0 (% OFLI 0) entries in Table 3. The diagnosed flare categories DFLI are designated by the category with the largest diagnosed probability for each sequence. Table 3 values indicate that the number of FLI 0 sequences is greatly under-represented in the diagnoses, meaning that there are an excessive number of flare false alarms. Diagnosis uncertainty values in Table 3, each of which is the individual sequence diagnosis uncertainty averaged over all sequences in the respective application set, show that the highest diagnosed probability is on average less than 0.5. This means that there is less of a chance that the diagnosed most-likely category is correct than that it is incorrect.  Finally, the large frequency distribution fit (FDF) values show that the diagnosed FLI categories for the sequences poorly represented the actual observed FLI frequency distribution. Improperly diagnosed FLI 0 sequences contributed greatly to this shortcoming.

**Table 3. Performance Metrics for the Whole Sequence Development/Application Process**

| Application Set | Brier Score | Bias | Diagnosis Uncertainty | FDF | % DFLI 0 | % OFLI 0 |
|---|---|---|---|---|---|---|
| 1 | 0.16 | 0.27 | 0.56 | 1.00 | 16.67 | 60.00 |
| 2 | 0.17 | 0.29 | 0.54 | 0.93 | 13.33 | 56.67 |
| 3 | 0.16 | 0.29 | 0.62 | 0.80 | 30.00 | 56.67 |

To gain a better understanding of how the frequency distribution of 1-minute eigenvector changes may have affected the diagnosis of FLI, we show the frequency distribution of the eight leading eigenvectors derived from the image sequences of development set 1_2 in Figure 12. The frequency distributions for the eigenvectors are shown separately for each FLI. Keep in mind that the size bins depend only on eigenvector and not on FLI, so they are the same in all FLI categories for a given eigenvector. We can immediately see a similarity between FLI 0 and 1,
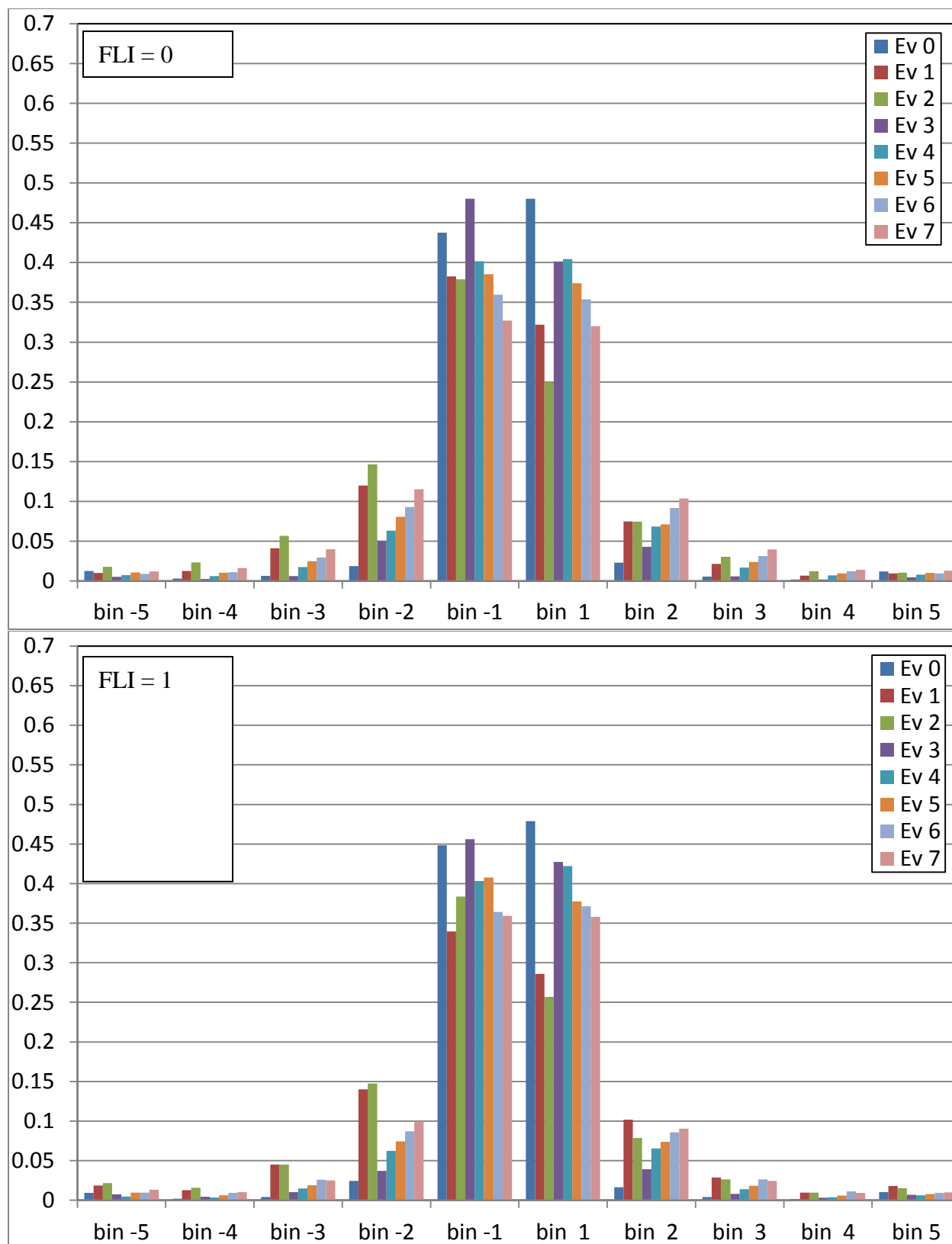
**Figure 12. Whole Sequence Method Frequency Distribution for Development Set 1_2**
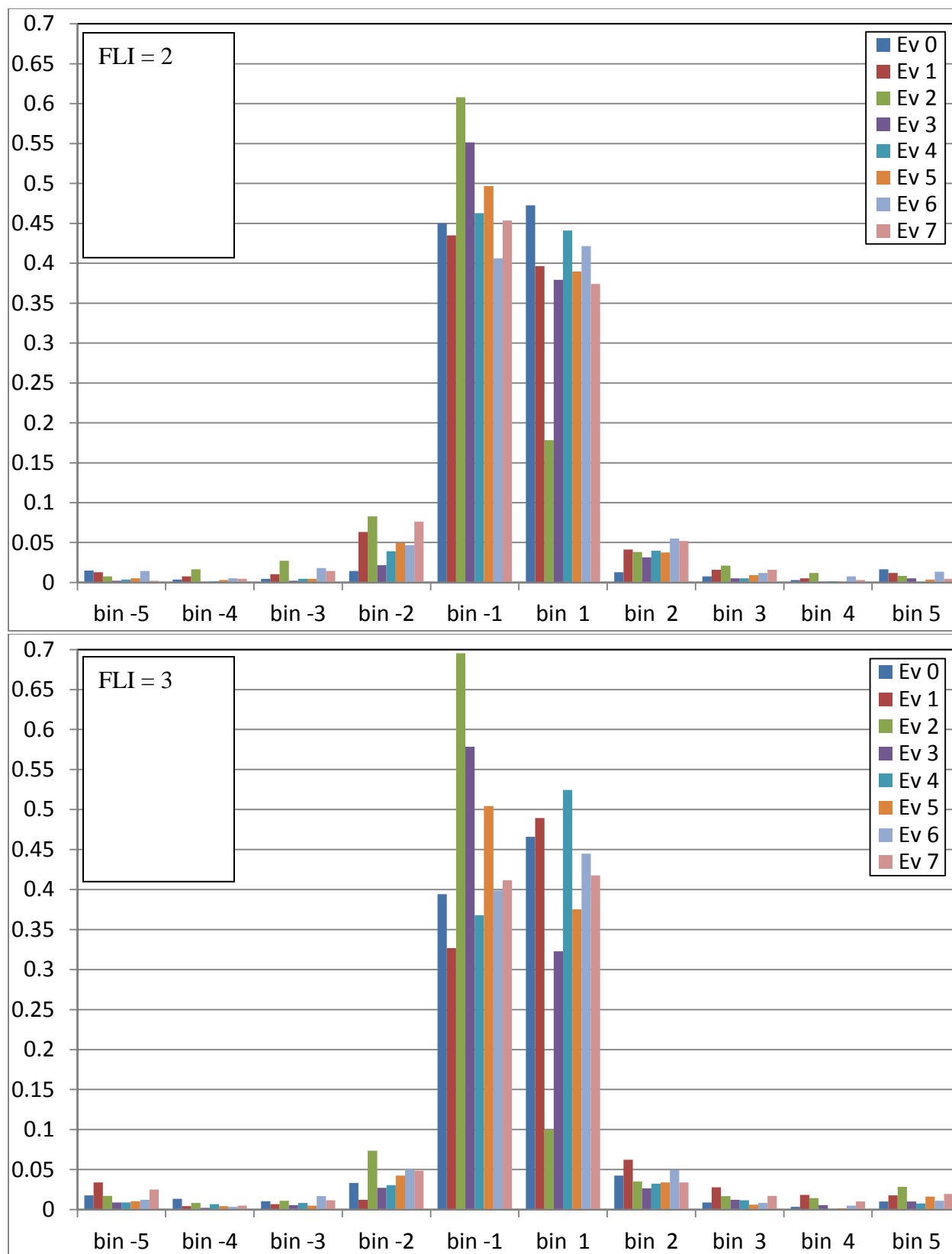
**Figure 12. (Cont.)**

25

and between 2 and 3. In FLI 0 and 1, the two smallest size bins have frequencies of occurrence of less than 0.5 for all eigenvectors, and $0.05 - 0.15$ for the next larger size bins on either size of zero. By contrast, in FLI 2 and 3 the frequency of occurrence extends well beyond 0.5 for some eigenvectors, and the two smallest size bins are much less symmetric about zero than in FLI 0 and 1. The larger size bins have smaller frequencies of occurrence for all eigenvectors in FLI 2 and 3, particularly bin -3, bin -2, bin 2 and bin 3. Because these frequency distributions are the basis for the discriminant vectors derived by the MVDA algorithm, we would expect a greater separation between FLI 0-1 and FLI 2-3 than we would between 0 and 1 and between 2 and 3.

When we diagnosed FLI for the image sequences of application set 3, we applied the derived discriminate vectors from development set 1_2 to the frequency distributions of the 1-minute eigenvector changes from each application image sequence. The frequency distributions from four selected sequences of application set 3 are shown in Figure 13. The chosen images sequences were: 20030203_10274 (OFLI 0), 20030528_10365 (OFLI 1), 20050506_10758 (OFLI 2), and 20061206_10930 (OFLI 3). The application of the discriminate vector to these frequency distributions of the 1-minute changes of eight leading eigenvectors yields a discriminant function value in discriminant space. A comparison of its position with respect to means of the four FLI groups determines the probability of each group. In the four charts of Figure 13, we indicate the diagnosed FLI (DFLI) and the observed FLI (OFLI) for the four selected sequences whose frequency distributions are displayed. We would expect that the FLI category of the development set having the 1-minute change eigenvector frequency distributions most similar to that of the particular application sequence would have been the one diagnosed for that sequence. We do see the greater frequencies of occurrence concentrated in the two smallest size bins in the OFLI 2 and 3 application sequences as expected. The fact that the OFLI 0 and 1 application sequences have substantial frequencies of occurrence in bin -2 and 2 unlike the OFLI 2 and 3 sequences should have placed these sequences closer to FLI 0 and 1 in the diagnosis. However, this was clearly not the case – both were diagnosed in discriminant space as lying closest to the group 3 mean, but not by much. In fact, the probability of FLI 3 was only 0.34 and 0.33 respectively, indicating a diagnosis uncertainty of 0.66 and 0.67. For the other two selected application sequences with DFLI 0 and 3 and OFLI 2 and 3, their probability of the DFLI categories were 0.29 and 0.53, or diagnosis uncertainty of 0.71 and 0.47. Clearly the level of discrimination among the FLI categories is low, and there is excessive ambiguity in the FLI classification of any application sequence.
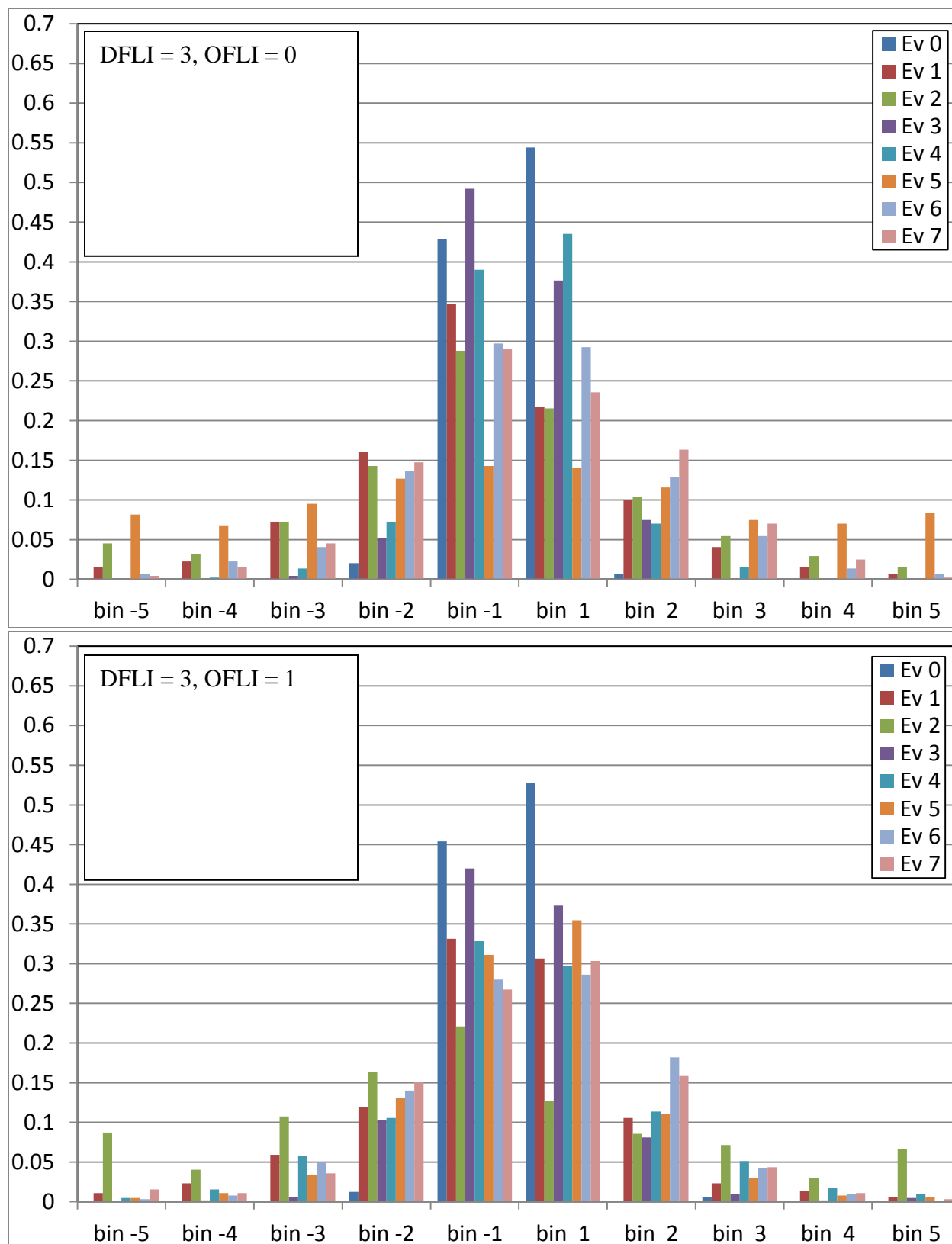
**Figure 13. Same as Figure 12 Except for Four Image Sequences of Application Set 3**
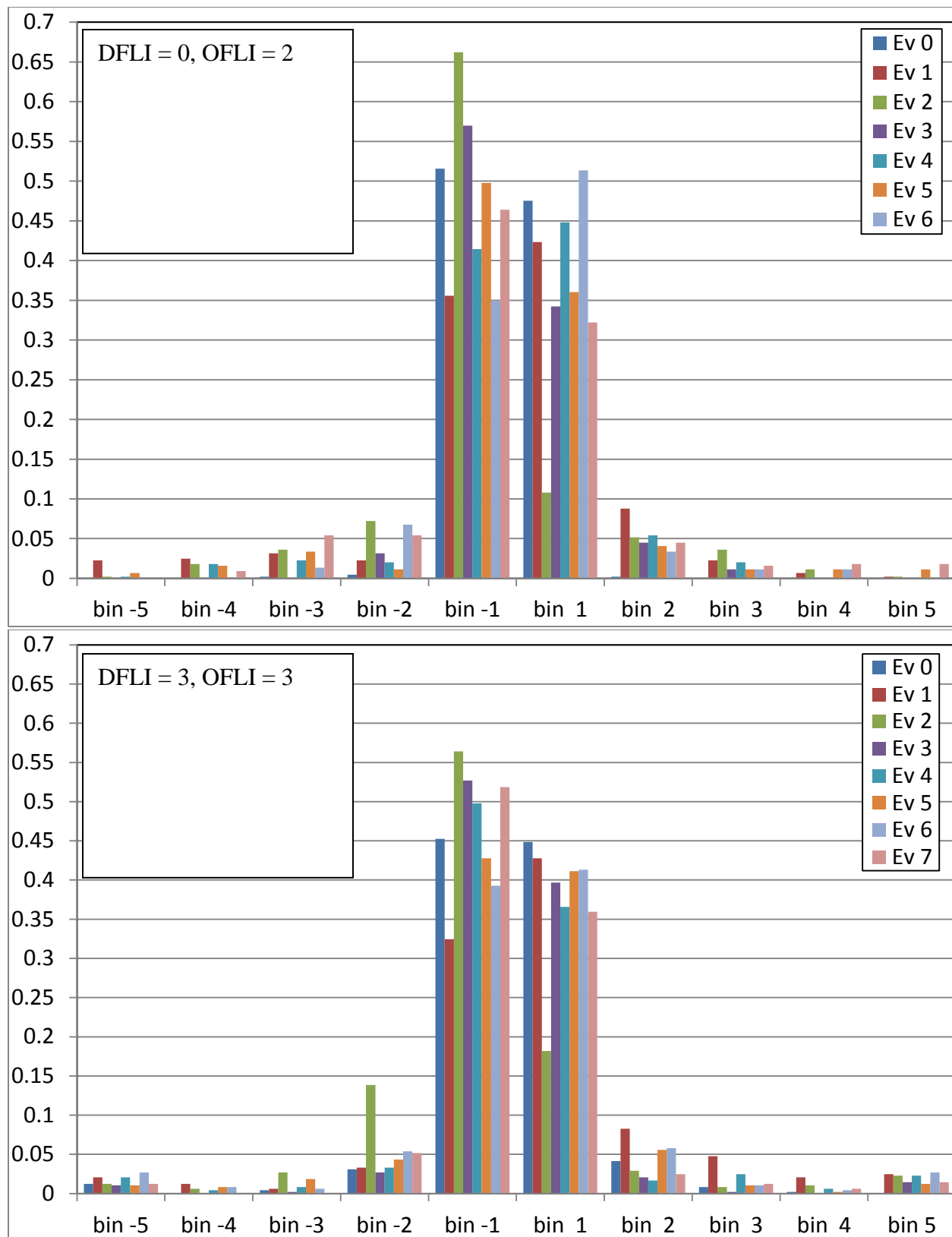
27

**Figure 13. (Cont.)**

There are two major reasons why the discrimination is lacking in this approach to classification of image sequences by FLI. First, there is too much similarity among the 1-minute eigenvector change frequency distributions partitioned by FLI as shown in Figure 12. The discriminant functions of the FLI group means lie too close together in discriminant space to indicate a clear distinction among them. The other major reason is that the 1-minute eigenvector change frequency distribution of any given application sequence is too dissimilar to any of the frequency distributions by FLI of the development sequences. Both of these possibilities suggest there is perhaps too much variation in the eigenvector patterns among the sequences of a particular FLI category. This precludes a distinct frequency distribution derived from the development sequences for each FLI category, and no strong resemblance of an application sequence frequency distribution to any of the FLI categories' frequency distributions.

## 6. PRE-FLARE ALGORITHM DEVELOPMENT/APPLICATION

In looking again at the eigenvector patterns by FLI group as exemplified by the selected image sequences in Figure 6-9, we see that the time period before the flare exhibits the greatest differences. After the flare, there are large oscillations in FLI 1-3 that could be confused with the sinusoidal swings present in FLI 0 (see, for example, Figure 4). We thought that by restricting the development of the discriminant vectors to just the pre-flare 1-minute eigenvector changes in the sequences with OFLI 1-3, we might be able to enhance the discrimination among the FLI groups. That is, we may get greater separation among the means of the discriminant functions of the four FLI groups. We revised the development algorithm to incorporate the method used in the Hα eigenvector – x-ray flux algorithm that determined the start time of the x-ray flux rise associated with the prescribed flare in each OFLI 1-3 sequence. We then used only the 1-minute eigenvector changes from the sequence start time up to that flare rise start time to determine the frequency distributions. Any sequence that had fewer than 100 1-minute change times before flare rise start was not allowed to contribute to the frequency distributions, and thus was not involved in determining the discriminant vectors in the MVDA algorithm. For OFLI 0 sequences, we continued to use all of the 1-minute eigenvector changes for the entire sequence in the frequency distributions. Therefore, the frequency distributions determined over all development sequences in a given development set will be the same as before for FLI 0, but should be more distinct for FLI 1-3.

In Figure 14, we show the frequency distributions determined from the altered development algorithm for the development set 1_2.  These can be compared with their counterparts from the whole sequence algorithm in Figure 12, keeping in mind changes in the size bin boundaries for some of the eigenvectors. The development data set had the following numbers of 1-minute changes that went into the frequency distributions by FLI category: for the original whole sequence algorithm: 16315, 8669, 1329, 1796 for FLI 0-3; for the pre-flare algorithm: 16315, 2533, 624, 982 for FLI 0-3. Of the 60 image sequences in development set 1_2, 54 met the minimum 100 1-minute change time requirement to participate in the algorithm. Looking at the new frequency distributions in Figure 14, we see that as with the whole sequence algorithm, the FLI 0 and 1 frequency distributions are quite similar. Both the FLI 2 and 3 are more different from the FLI 0 and 1 frequency distributions than they were for the whole sequence algorithm.
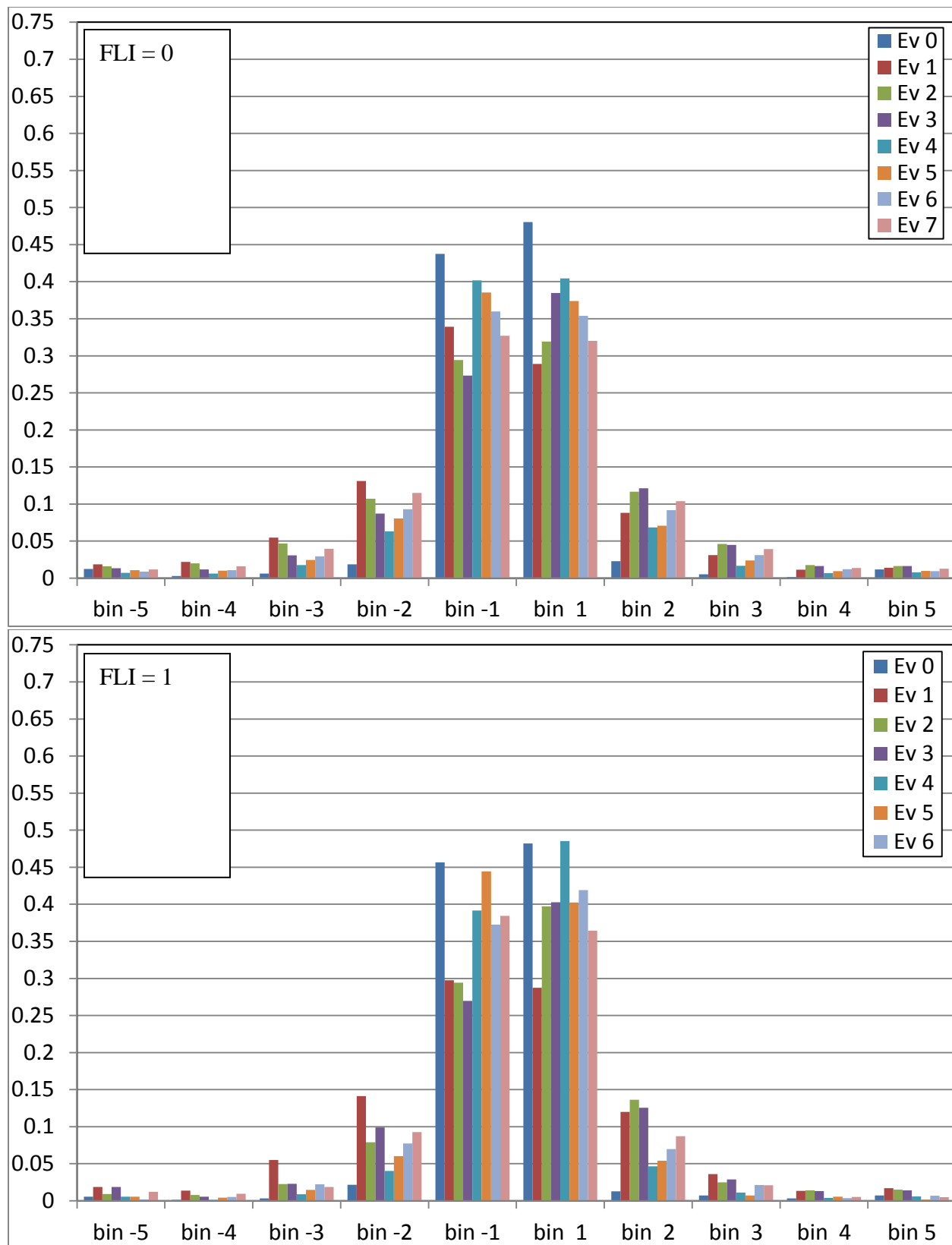
**Figure 14. Pre-Flare Method Frequency Distribution for Development Set 1_2**

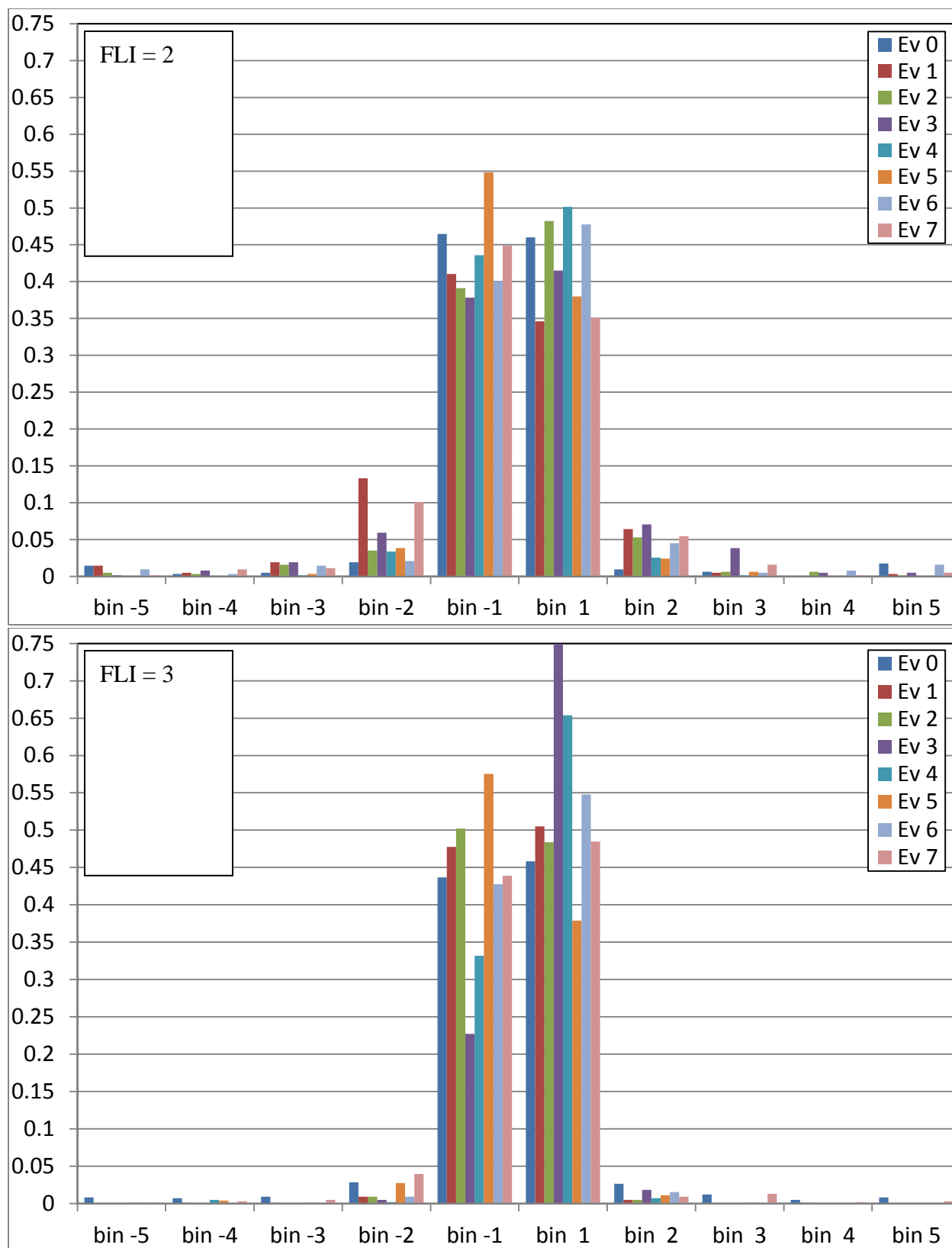Approved for public release; distribution is unlimited.

**Figure 14. (Cont.)**

More of the frequency of occurrence is concentrated in the bin -1 and 1 bins, and some of the outlying bins have very little representation by any of the eigenvectors. The distributions for FLI 2 and 3 are different in that there is more variation with eigenvector in the two central bins in the latter. This was also true for FLI 2 and 3 in the whole sequence algorithm. It is hard to determine to what extent we achieved our goal of greater distinction among the frequency distributions of the four FLI categories at this point – only that it seems we achieved a greater FLI 0-1 and FLI 2-3 difference.

We then applied the discriminant vectors from the pre-flare development algorithm to the respective application sets. We maintained the restriction of using only the pre-flare image times to construct the frequency distribution of 1-minute eigenvector changes for each OFLI 1-3 application sequence. For the OFLI 0 sequences, we used the image times before the hour nearest the mid-time of the sequence period.  We diagnosed FLI category probabilities only for the application sequences that had at least 180 image times resulting from these restrictions. This eliminated nine of the 30 application sequences from being diagnosed for FLI category probability. We selected the same four sequences from application set 3 to show the frequency distribution of 1-minute eigenvector change frequency distributions in Figure 15. For perspective, the number of 1-minute changes making up the frequency distributions of the four sequences were 441, 643, 444, 484 for the OFLI 0-3 sequences respectively for the whole sequence algorithm (whose frequency distributions are shown in Figure 13), and 244, 286, 193, 199 for the OFLI 0-3 sequences respectively for the pre-flare algorithm (whose frequency distributions are shown in Figure 15). We gained the perceived advantage of greater distinction by FLI category in the development set frequency distributions, but suffered the disadvantage of fewer 1-minute change values going into the frequency distributions in both development and application. Frankly, the OFLI 0 application sequence frequency distribution in Figure 15 is very irregular and does not resemble any of the four frequency distributions of the development sequences as shown in Figure 14. Eigenvectors 1-3 have smaller frequencies of occurrence in bins -1 and 1 for the OFLI 1 application sequence (Figure 15) than for the OFLI 1 development sequences (Figure 14). Even so, the collective frequency distributions overall clearly resemble FLI 1 more than FLI 3 (see Figure 14), yet the latter was indicated as most likely. The OFLI 2 sequence (Figure 15) is a complete mystery to us – if anything, it looks more like the FLI 3 frequency distribution of the development sequences, certainly not FLI 1 which was what was diagnosed as most likely. Finally, it is more understandable that the OFLI 3 application sequence could be confused with the FLI 2 development sequences' frequency distributions, since they are similar to the FLI 3 frequency distributions.
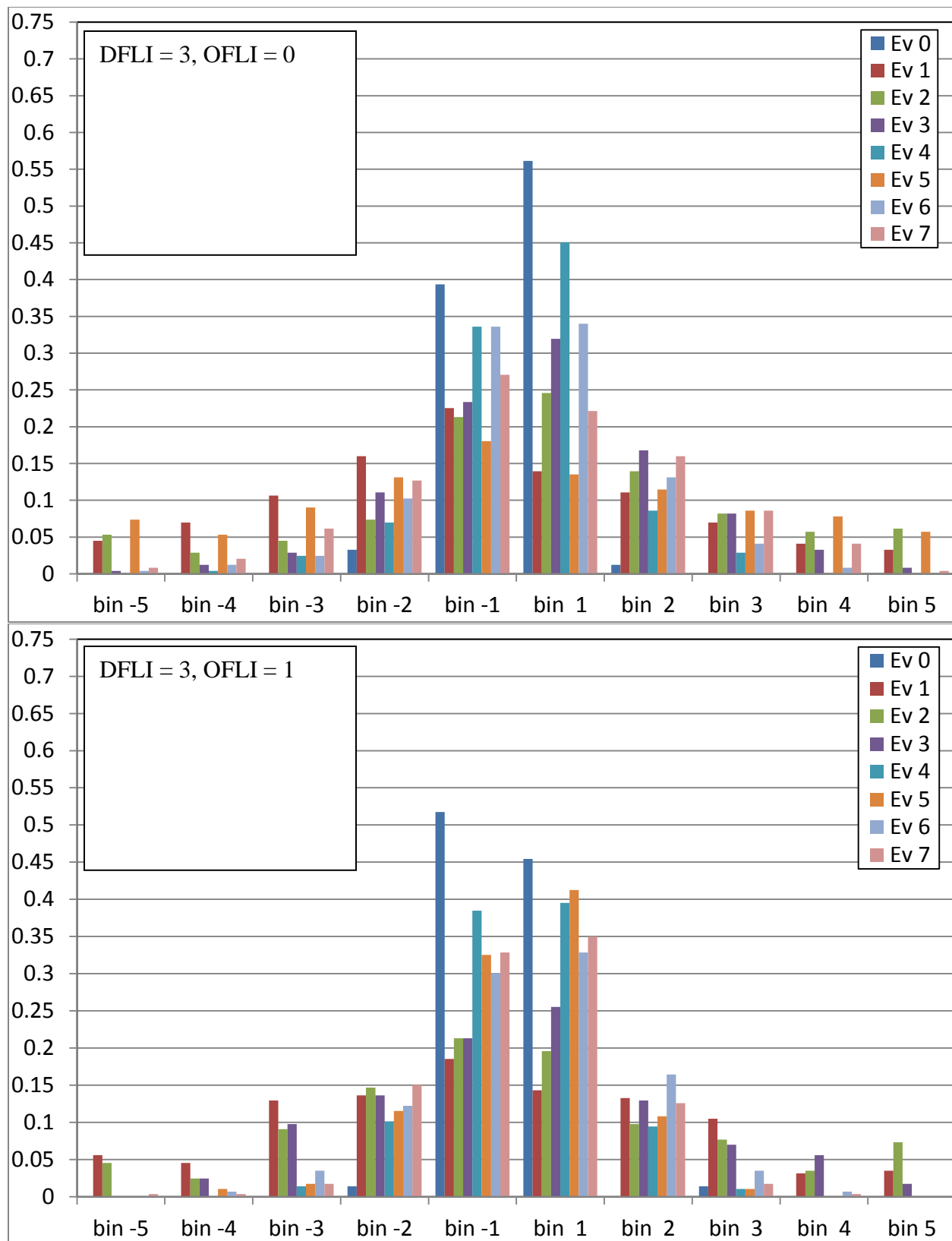
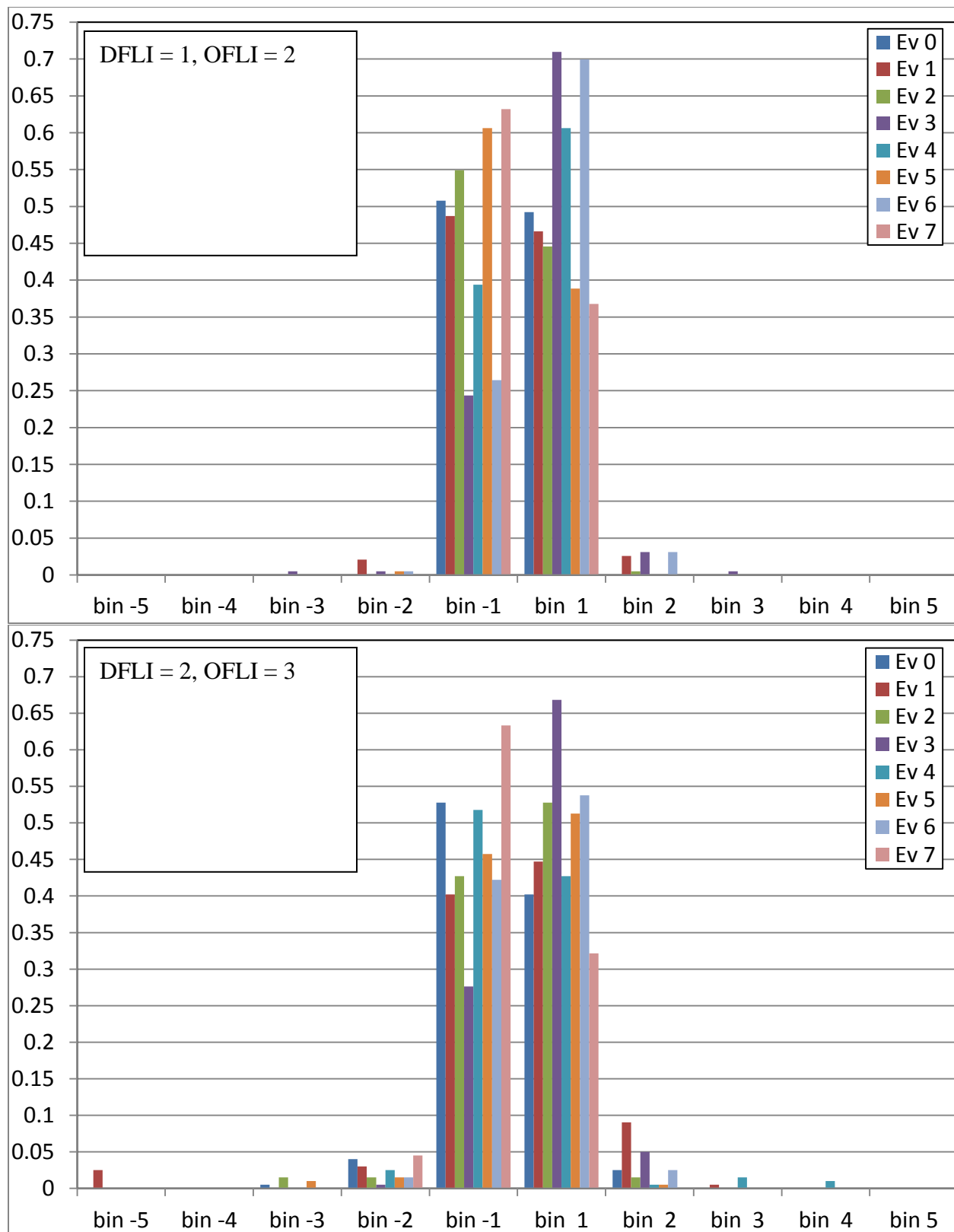**Figure 15. Same as Figure 14 Except for Four Image Sequences of Application Set 3**

**Figure 15. (Cont.)**

It appears that in employing the pre-flare version of the development and application algorithms, we suffer from a smaller pool of 1-minute eigenvector changes (minimum of 180) from which to construct the frequency distributions for each application sequence. Therefore, they are less representative of the frequency distributions created from the 1-minute eigenvector changes of the development sets' sequences. We did not seem to profit from focusing on just the pre-flare eigenvector information, even though it was more distinct by flare category than using 1-minute eigenvector changes from the entire sequences.

In Figure 16 we show the probability-weighted diagnosed flaring categories for those sequences for which the minimum 180 image times was satisfied vs. the OFLI. In comparing these plots with those from the whole sequence approach in Figure 11, we see that again most of the PWDFC values are in the flaring category 1-2 domain. The pre-flare algorithms did not improve the ability to properly diagnose the FLI 0 (non-flaring) sequences. Also as with the whole sequence method, there is no obvious association of sequence-to-sequence variation between PWDFC and OFLI. We list the performance metrics results for the pre-flare development and application algorithms in Table 4. Numbers in parentheses in the "Application Set" column denote the number of application set sequences (out of 30) that had at least 180 image times to construct the frequency distributions. The results for application sets 1 and 3 are actually worse than for the whole sequence method as shown in Table 3, while application set 2 has values that are competitive. The level of positive bias, serious lack of FLI 0 diagnoses, and the large FDF in application sets 1 and 3 suggest that the liability of having fewer image times to construct the frequency distributions overcame the advantage of greater category distinction in the use of just pre-flare image times.
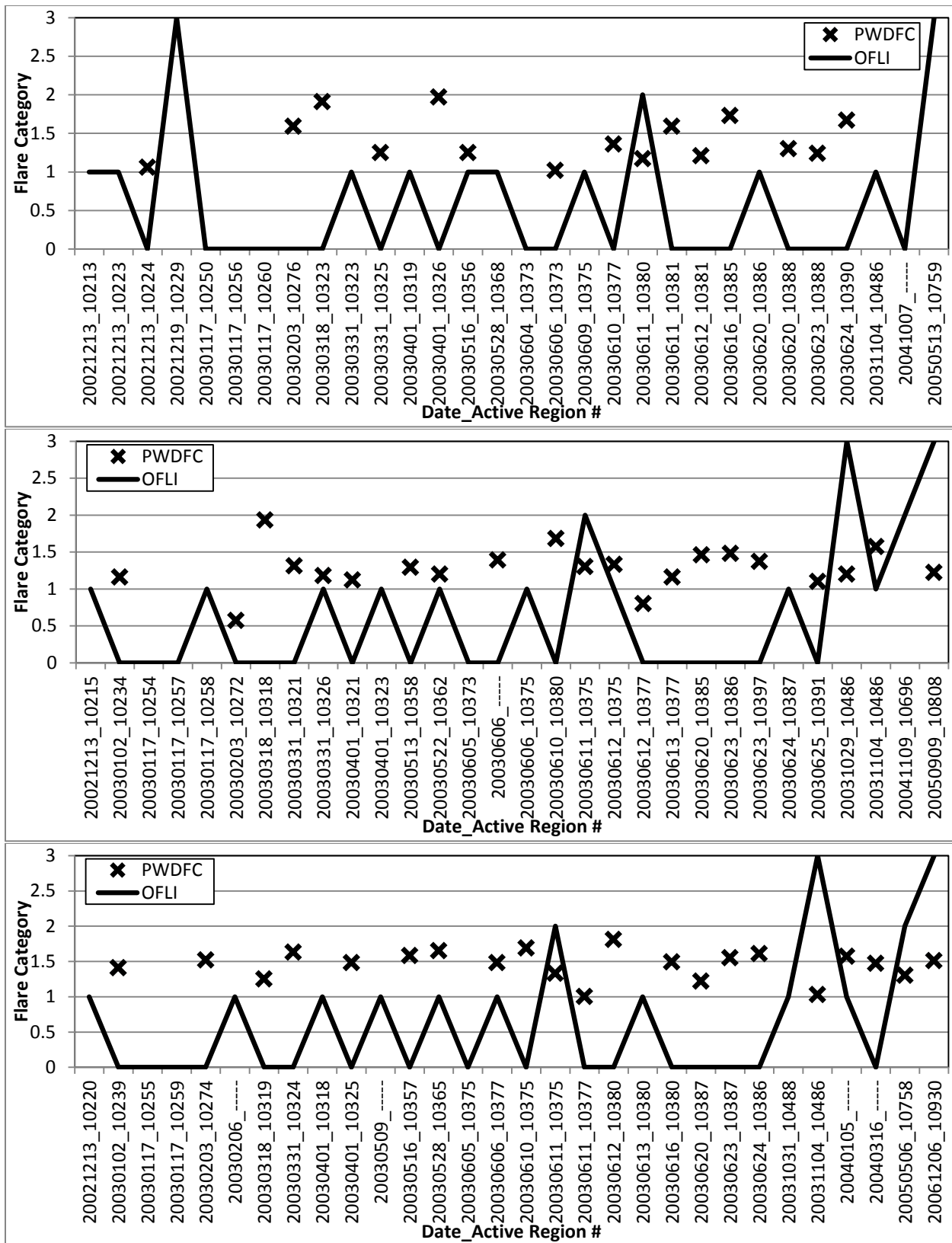
**Figure 16. Pre-Flare Method PWDFC vs. OFLI for Application Sets (1), (2), (3)**

**Table 4. Performance Metrics for the Pre-Flare Development/Application Process**

| Application Set | Brier Score | Bias | Diagnosis Uncertainty | FDF | % DFLI 0 | % OFLI 0 |
|---|---|---|---|---|---|---|
| 1 (15) | 0.22 | 0.41 | 0.54 | 1.73 | 0.00 | 86.67 |
| 2 (21) | 0.17 | 0.24 | 0.59 | 0.29 | 57.14 | 66.67 |
| 3 (21) | 0.21 | 0.28 | 0.56 | 1.24 | 4.76 | 66.67 |

# 7. ISOON DOPPLER VELOCITY AS FLARE PREDICTORS

At the end of the current study period, we considered the use of Doppler velocity signal in the ISOON image pixels as a possible way to augment the flare indicator information from the Hα images. At one-minute intervals, the plasma speed in the chromosphere toward (away from) the viewer is represented by blue (red) shift in the wavelength of received light. The degree of shift from the center line wavelength indicates the speed, which we refer to as the Doppler velocity. We processed one-minute interval Doppler velocity in each ISOON image pixel over the same sub-regions of solar active regions processed for ISOON Hα. Processing included extracting the data in the sub-regions from the whole disk image. After extraction, the images were normalized, spatially oriented and aligned. We then applied principal component analysis (PCA, e.g., see Wilks [3]) to each of the sub-region sequences of one-minute interval Doppler velocity grids. In this way, the eigenvectors and eigenvalues were derived in a manner directly analogous to the processing conducted on the one-minute interval Hα image sequences.

In Figures 17-20, we show the nine leading eigenvectors and the cumulative explained variance as derived from all of the eigenvalues for four image sequences. These are the same sequences for which we showed the leading Hα eigenvectors in Figures 4, 6, 8, and 9 respectively. A five-point smoother has been applied to the eigenvectors in both sets of figures. Note the difference in the time span of the data between the Hα and Doppler velocity figures.

In comparing the leading Hα (Figure 4(a)) and Doppler velocity (Figure 17(a)) eigenvectors from FLI 0 image sequence 20030117_10250, we see a pervasive sinusoidal pattern in the former which only becomes apparent with eigenvector 2 and higher in the latter. With the imposed smoother acting on both sets, it is clear that there is much more high frequency variation in the Doppler velocity eigenvectors than for the Hα eigenvectors. This may also be reflected in the explained cumulative variance shown for the Doppler velocity in Figure 17(b). While we found that 99.9% of the explained variance was achieved consistently by about the first 50 Hα eigenvectors and often many fewer than that, here we see that for this sequence it is only attained at the highest order eigenvectors. The curving Hα eigenvector patterns of Figure 6(a) contrast with the flat Doppler velocity eigenvectors shown in Figure 18(a) for the FLI 1 sequence 20030522_10362. With the plentiful vertical spikes in the Doppler velocity eigenvector curves it is difficult to associate any particular inflection with the obvious flare inflection between 20 and 22 UTC in the Hα eigenvectors. Comparing Hα eigenvectors in Figure 8(a) with Doppler velocity eigenvectors in Figure 19(a) for the FLI 2 sequence 20050506_10758 reveals an extremely different signature. The Hα eigenvectors show the classic FLI 2 gently curving pre-flare shape with the deep drop and rise associated with the flare. The Doppler velocity eigenvectors display no obvious sign of the flare occurring between 16 and 18 UTC, and in fact their sinusoidal patterns are similar to those of the FLI 0 Hα eigenvectors. Even more dramatic is
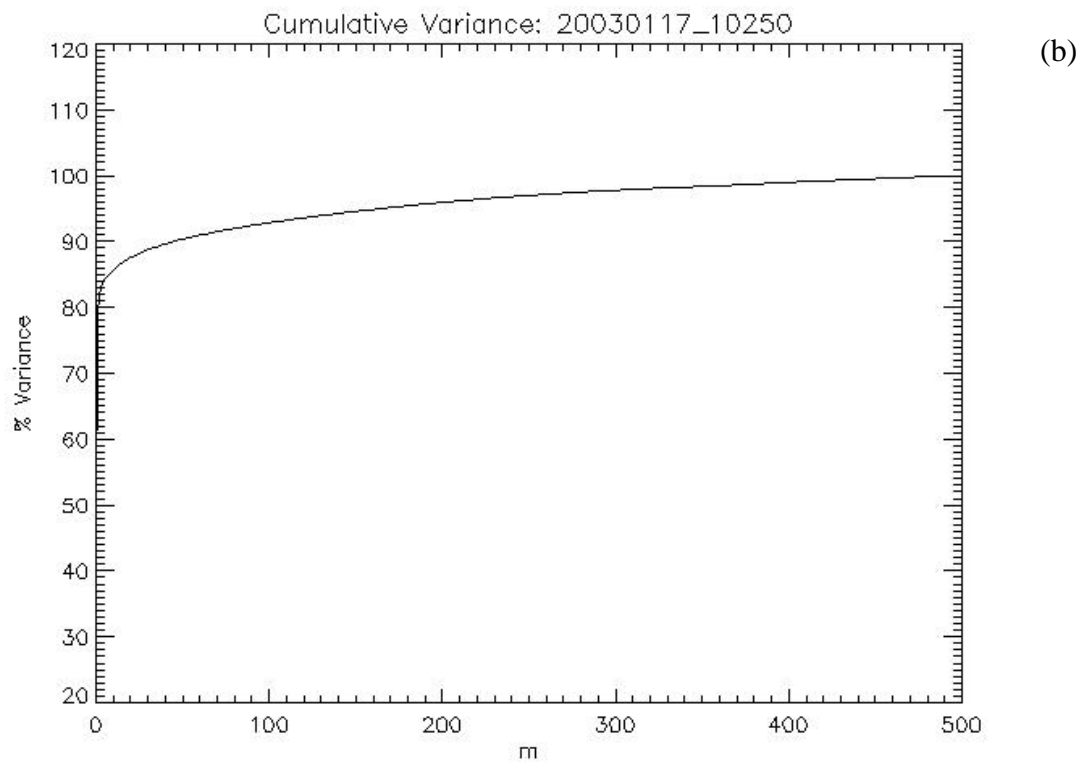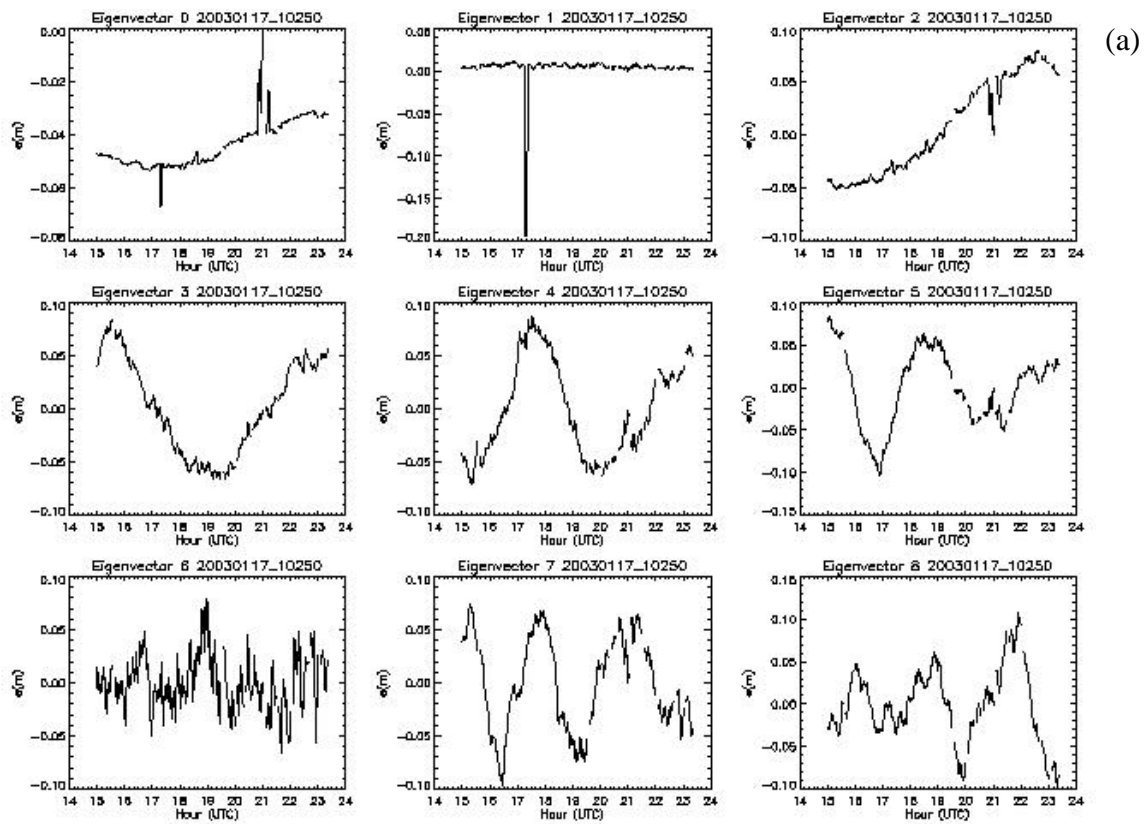
**Figure 17. 20030117_10250 Doppler Velocity (a) 1st 9 Eigenvectors, (b) Explained Variance**
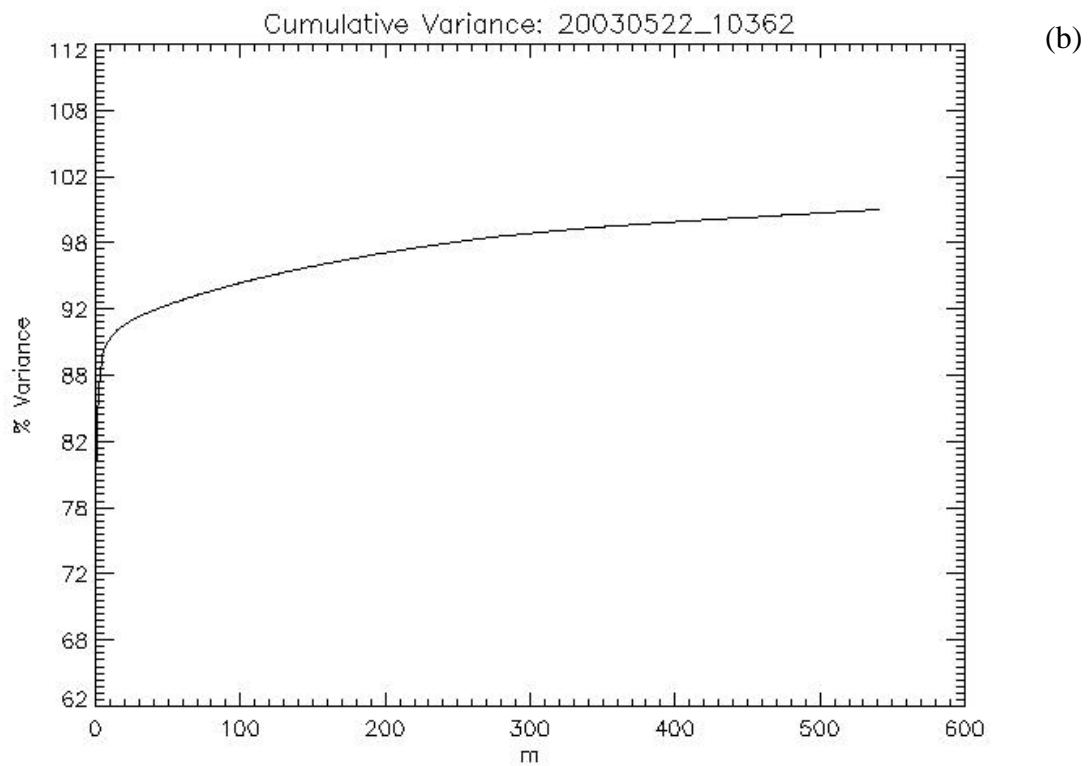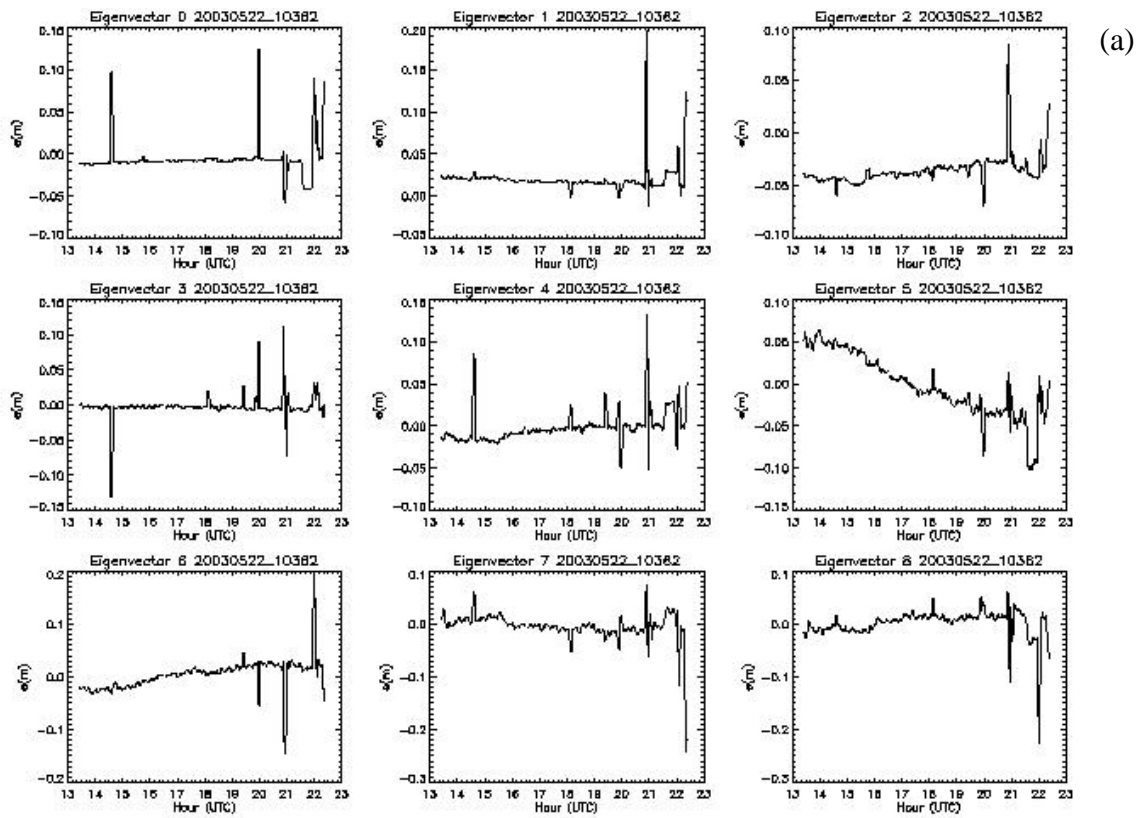
38

(a)

(b)

**Figure 18. Same as in Figure 17 Except for 20030522_10362**
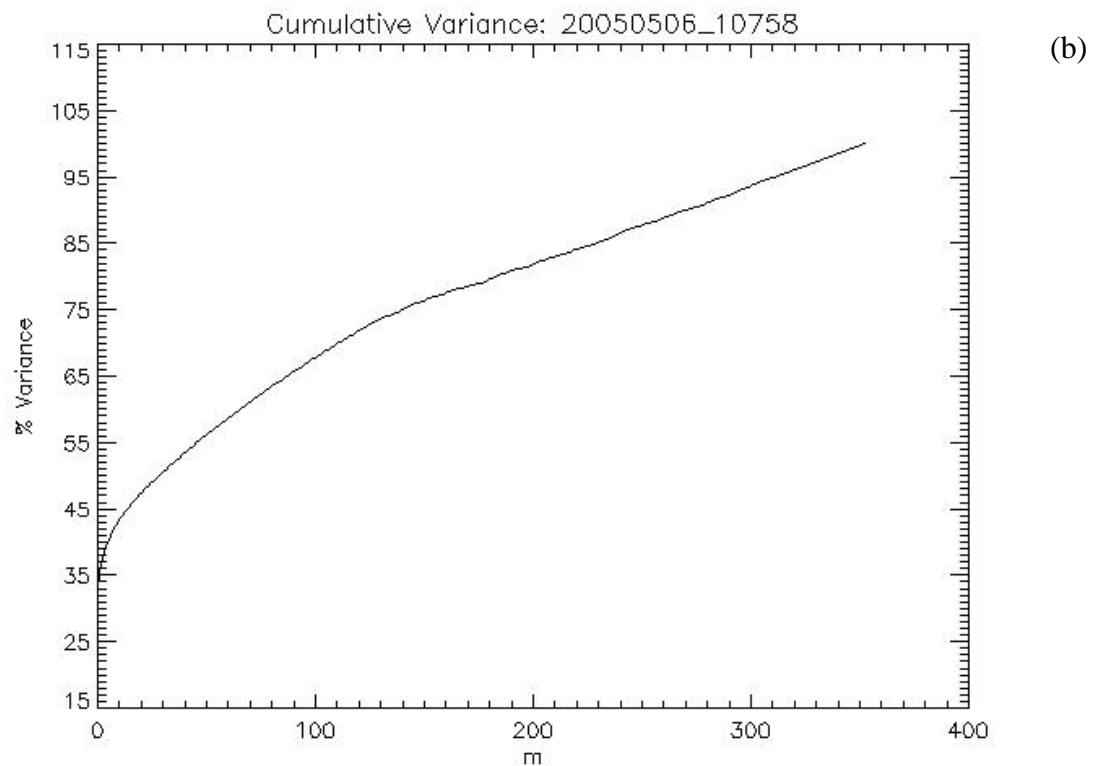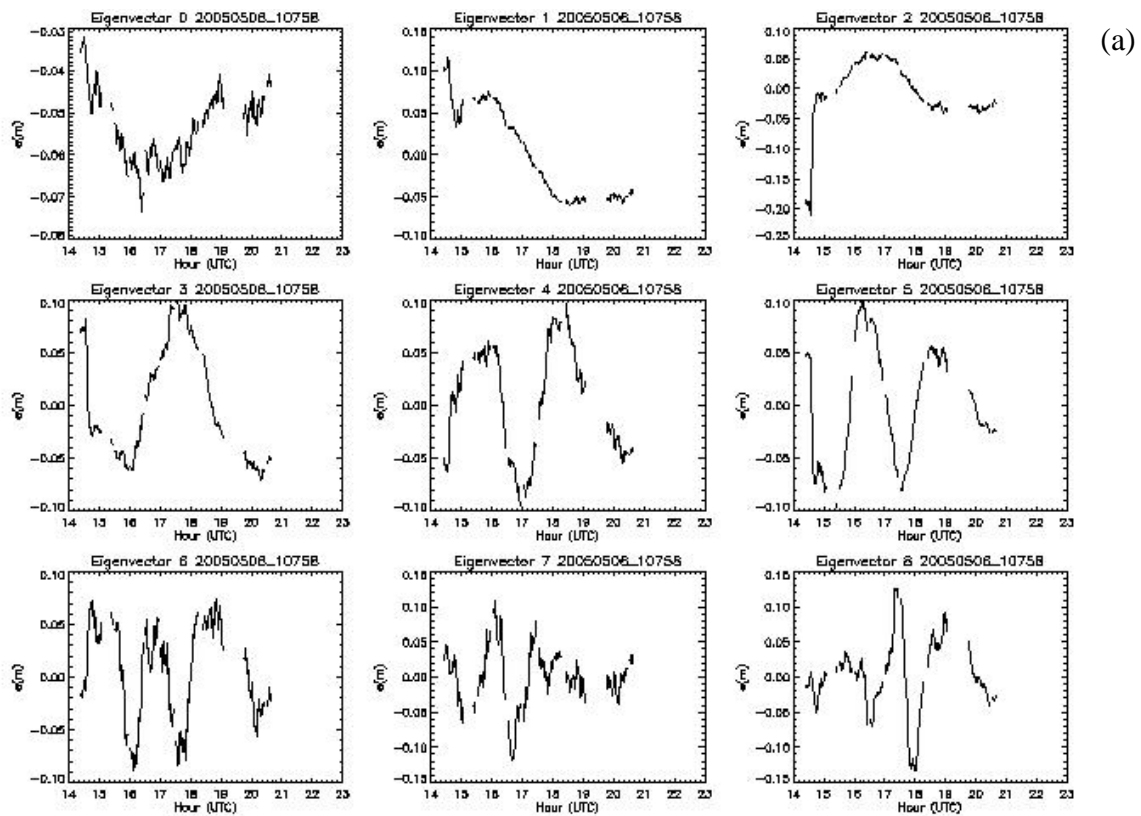
(a)

(b)

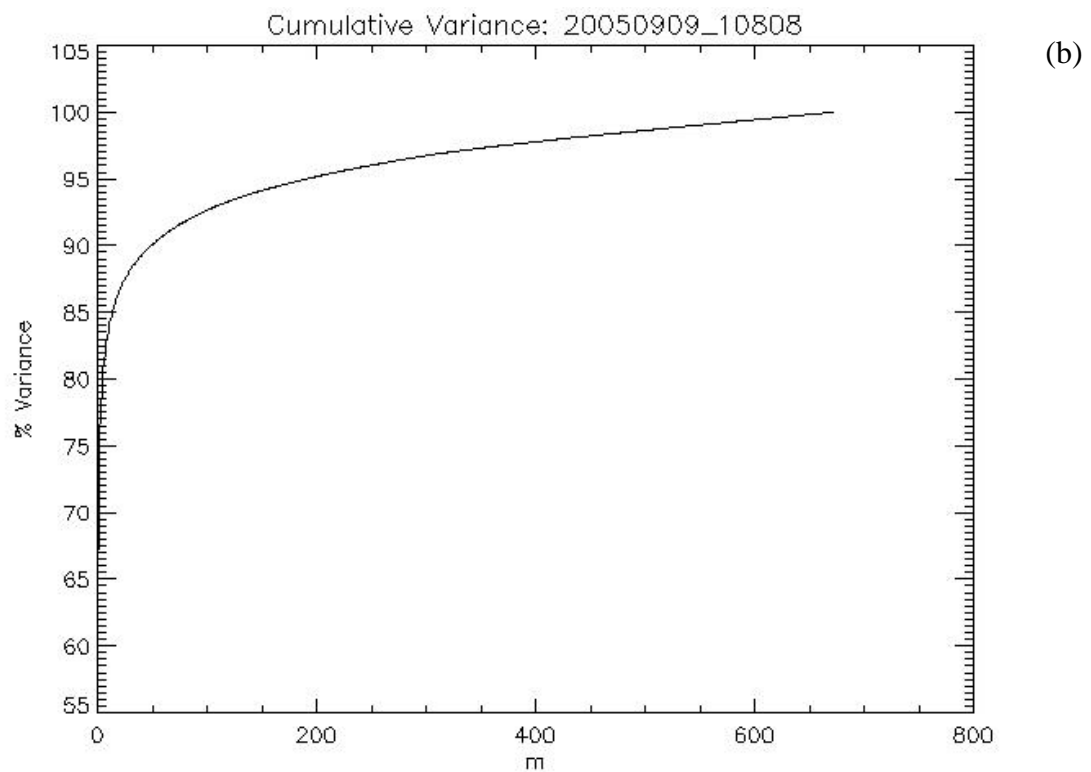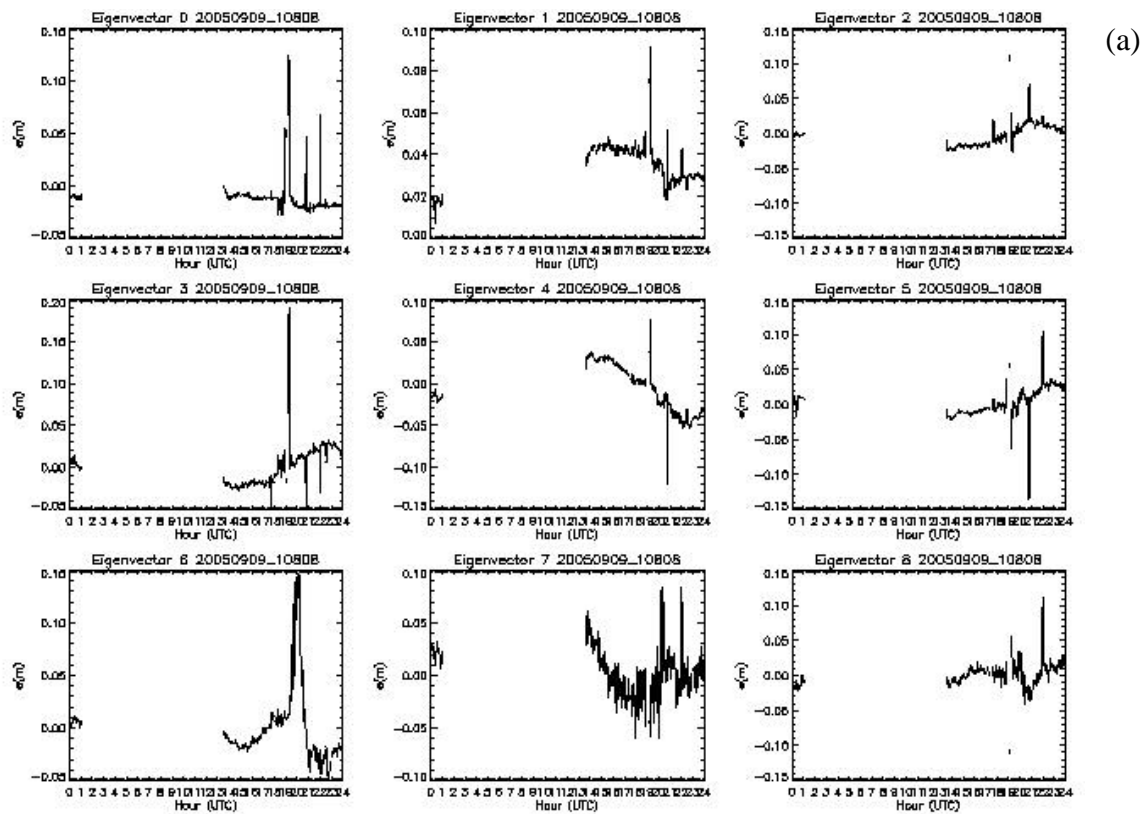**Figure 19. Same as in Figure 17 Except for 20050506_10758**

**Figure 20. Same as in Figure 17 Except for 20050909_10808**

the slow rise of cumulative explained variance as shown in Figure 19(b). About 300 Doppler velocity eigenvectors are required to represent 95% of the variance. Finally, in comparing the Hα and Doppler velocity eigenvectors for FLI 3 sequence 20050909_10808 in Figures 9(a) and 20(a) respectively, we see a similar relationship between the patterns. The very clear signature of the flare in the Hα eigenvectors is largely absent in the Doppler velocity eigenvectors, though we do see a large rise in eigenvector 6 at about the expected rise time of the flare. In this case we see about 95% of the variance explained by the first 200 eigenvectors.

It appears from this admittedly limited number of examples that more of the temporal variation in the Doppler velocity is carried at much higher order eigenvectors than for Hα. This seems to suggest that the Doppler velocity is a more spatially and temporally variant, or noisier, field than the Hα imagery. We found in this study that the variation in eigenvector patterns among image sequences of a particular FLI category limit the ability of the MVDA flare probability diagnosis technique. We would surmise that the even more variant Doppler velocity would not benefit the process. In addition, it appears that many more eigenvectors would be required to capture enough of the explained variance to fully represent the physical phenomenon. It may be that the Doppler velocity may have information to contribute to flare diagnosis and maybe even prediction. However, investigating this potential benefit would require another project on the scale of the present one conducted on Hα imagery. It is clear from this limited analysis that Doppler velocity cannot suitably augment Hα imagery in the flare diagnosis techniques developed and used in this study.

## 8. SUMMARY AND CONCLUSIONS

The current study period was a sequel to the original study of the diagnosis of flare probability that began in mid-2009. The focus of the entire effort was to see if high-cadence Hα imagery could be used to detect, and ultimately predict, solar flares. We made two major choices of tools to investigate this possibility. First, we subjected the selected sequences of Hα images to Principal Component Analysis to derive the eigenvectors and eigenvalues of the one-minute interval grids of pixel values. Second, we chose multivariate discriminant analysis as the data-driven statistical technique to derive relationships between predictors (Hα data in the form of eigenvectors) and predictands (degree of flaring). Ultimately we settled on four degrees of flaring, or flaring level indicators, for the predictand categories. We noticed that the temporal patterns of the leading eigenvectors from the selected sequences seemed to fall into these four groups. At the same time, the four groups were independently corroborated by peak x-ray flux associated with the corresponding degree of flaring. We used the combination of leading eigenvector patterns and peak x-ray flux to assign each of the selected sequences to the four flaring categories. It then remained to determine the most effective way to stage the associated predictor vectors in order to optimize diagnosis of flare category probability.

In this study, we tried two methods involving individual image time flare category probability diagnosis. First, we employed the legacy flare category probability development and application algorithms from the original study. This used the straight eigenvector values from 25-50 leading eigenvectors as the elements of the predictor vectors at each image time. Area-averaged Hα of the sub-region from which the images were extracted, along with x-ray flux at the same one-minute time intervals served to identify the rise times of the flare if present. It was at these times

that predictands associated with the prescribed flaring level were assigned. Predictor vectors paired with the predictand for all image times in 60 image sequences went into the discriminant analysis routine. The resulting discriminant vectors were applied to 30 independent image sequences of individual image time predictor vectors derived from the leading eigenvectors. The probability of each of the four flaring categories was diagnosed at each application image time. Comparing them with the prescribed flaring level category (non-zero only at flare rise times) yielded statistical metrics that measured the diagnosis performance.

We devised a second individual image time flare category probability diagnosis method by modifying the first one in two major ways. First, we used one-minute changes in the leading eigenvectors as predictors in place of the full eigenvector values. Second, we eliminated use of area-average Hα intensity to set the flare rise times, relying solely on x-ray flux.

In terms of the statistical metrics by which we gauged flare category probability diagnosis performance, the two individual image time methods performed about the same. The probability-weighted diagnosed flare category at each time was compared with the observed flaring category in computing Brier Score (essentially mean squared difference), Bias, and what we called Diagnosis Uncertainty. The latter was the average over all image times of one-minus-largest category probability. Both methods showed a consistent positive bias, indicating a tendency to produce false alarms. In some non-flaring sequences, there was a tendency to diagnose an excessive number of times indicating weak flaring. Also, because of an insufficient degree of discrimination among the flaring categories, diagnosis uncertainty was unacceptably large, averaging 39 to 48 percent depending on the method and set of development and application image sequences used. This means that the largest of the four category probabilities diagnosed was typically 52 to 61 percent – not nearly as definitive as would be desired. Neither of the two individual image time methods could create enough distinction among the four flaring categories to avoid frequent misdiagnosis, especially of flaring when the sub-region was not flaring.

A brief analysis of why some sequences were diagnosed well when others weren't seemed to indicate that there was significant variation of the eigenvector patterns within each flaring category. This is a common problem in discriminant analysis – excessive within-group scatter. It is not clear that this would be remedied by developing the technique over more image sequences. It might only broaden the range of predictor pattern variations. Another issue was that rises and falls in the eigenvector curves of the non-flaring sequences would be mistaken for flare-related inflections when the flaring category probabilities were determined. Again, there just wasn't enough distance in discriminant space between the four groups to clearly delineate the flaring category associated with an independent predictor vector.

We tried a radically different approach to flare category diagnosis by involving the image sequence as a whole rather than trying to diagnose at individual image times. We represented the patterns of the leading eigenvectors through frequency distributions of their one-minute interval changes. The predictor vector elements for a given image sequence were the ten bin values of frequency of occurrence of one-minute change for eight leading eigenvectors. We used the prescribed flaring category as the predictand for the image sequence. Again, the degree of distinction among the flaring categories fell short. The collective frequency distributions among the four flaring categories were insufficiently distinct to produce a clearly indicated most likely

43

flaring category. In fact, the diagnosis uncertainty was even greater than with the individual image time diagnosis methods. We even limited specifying predictor elements from frequency of occurrence to the image times prior to the flares, since the differences among the flaring categories seemed more distinct during those times. But this resulted in fewer image times from which to derive the frequency distribution, making them even more variable among the sequences, so the technique was less able to discriminate.

Our original ultimate goal in this endeavor was to be able to predict flaring from the high-cadence ISOON data. Unfortunately, we were not able to achieve a high enough level of flare diagnosis skill to go beyond that level. We still feel that the apparent distinction among the flaring categories as evident in the Hα eigenvectors may have potential for useful short-term flare prediction. However, we feel that we have reached the limit in achieving that goal insofar as applying multivariate discriminant analysis. In the future, other data-driven statistical techniques will be implemented in order to try to capitalize on that potential.

# REFERENCES

[1] Norquist, D. C., and K. S. Balasubramaniam, *Diagnosis of Solar Flare Probability from Chromosphere Image Sequences*, AFRL-RV-PS-TP-2011-0005, Air Force Research Laboratory, Space Vehicles Directorate (AFMC), Kirtland AFB, NM, Sep 2011.

[2] Neidig, D., et al, "The USAF Improved Solar Observing Optical Network (ISOON) and its impact on solar synoptic data bases," *Synoptic Solar Physics*, Astronomical Society of the Pacific Conference Series, K. S. Balasubramaniam, J. W. Harvey and D. M. Rabin, eds., **140**, 1998, pp. 519-528.

[3] Wilks,  D. S.,  **Statistical Methods in the Atmospheric Sciences, Second Edition**, Academic Press, Burlington, MA, 2006, 627 pp.

DISTRIBUTION LIST

DTIC/OCP
8725 John J. Kingman Rd, Suite 0944
Ft Belvoir, VA 22060-6218                    1 cy

AFRL/RVIL
Kirtland AFB, NM 87117-5776                   2 cys

Official Record Copy
AFRL/RVBXS/Donald Norquist                    1 cy